The African monsoon during the early Eocene from the DeepMIP simulations

Charles J. R. Williams[1,2], Daniel J. Lunt[1], Ulrich Salzmann[3], Tammo Reichgelt[4], Gordon N. Inglis[5], David R. Greenwood[6], Wing-Le Chan[7], Ayako Abe-Ouchi[7], Yannick Donnadieu[8], David K. Hutchinson[9,10], Agatha M. de Boer[9], Jean-Baptiste Ladant[11], Polina A. Morozova[12], Igor Niezgodzki[13,14], Gregor Knorr[14], Sebastian Steinig[1], Zhongshi Zhang[15], Jiang Zhu[16], Matthew Huber[17], Bette L. Otto-Bliesner[16]

[1]School of Geographical Sciences, University of Bristol, UK
[2]NCAS / Department of Meteorology, University of Reading, UK
[3]Geography and Environmental Sciences, Northumbria University, UK
[4]Department of Geosciences, University of Connecticut, US
[5]School of Ocean and Earth Science, University of Southampton, UK
[6]Department of Biology, Brandon University, Canada
[7]Atmosphere and Ocean Research Institute, The University of Tokyo, Japan
[8]Laboratoire des Sciences du Climat et de l'Environnement, France
[9]Department of Geological Sciences, Stockholm University, Sweden
[10]Climate Change Research Centre, University of New South Wales, Australia
[11]Earth and Environmental Sciences, University of Michigan, US
[12]Institute of Geography, Russian Academy of Sciences, Russia
[13]Institute of Geological Sciences, Polish Academy of Sciences, Poland
[14]Alfred Wegener Institute for Polar and Marine Research, Germany
[15]Bjerknes Centre for Climate Research, University of Bergen, Norway
[16]Climate and Global Dynamics Laboratory, National Center for Atmospheric Research, US
[17]Department of Earth, Atmospheric and Planetary Sciences, Perdue University, US

Corresponding author address: School of Geographical Sciences, University Road, Bristol, BS8 1SS, UK
Email: c.j.r.williams@bristol.ac.uk

Short title: Early Eocene simulations of the African monsoon

Keywords: Palaeoclimate, DeepMIP, Early Eocene, African monsoon, precipitation

KEY POINTS

1) State-of-the-art climate models are used to study African hydroclimate during the early Eocene (approximately 50 million years ago).
2) With increasing levels of CO_2, there are changes to African precipitation, due to dynamical changes such as low level circulation.
3) A comparison between the models and newly-compiled climate estimates shows a marginally better match at lower levels of CO_2.

ABSTRACT

The early Eocene (~56-48 million years ago) is characterised by high CO_2 estimates (1200-2500 ppmv) and elevated global temperatures (~10 to 16°C higher than modern). However, the response of the hydrological cycle during the early Eocene is poorly constrained, especially in regions with sparse data coverage (e.g. Africa). Here we present a study of African hydroclimate during the early Eocene, as simulated by an ensemble of state-of-the-art climate models in the Deep-time Model Intercomparison Project (DeepMIP). A comparison between the DeepMIP pre-industrial simulations and modern observations suggests that model biases are model- and geographically dependent, however these biases are reduced in the model ensemble mean. A comparison between the Eocene simulations and the pre-industrial suggests that there is no obvious wetting or drying trend as the CO_2 increases. The results suggest that changes to the land sea mask (relative to modern) in the models may be responsible for the simulated increases in precipitation to the north of Eocene Africa, whereas it is likely that changes in vegetation in the models are responsible for the simulated region of drying over equatorial Eocene Africa. There is an increase in precipitation over equatorial and West Africa and associated drying over northern Africa as CO_2 rises. There are also important dynamical changes, with evidence that anticyclonic low-level circulation is replaced by increased south-westerly flow at high CO_2 levels. Lastly, a model-data comparison using newly-compiled quantitative climate estimates from palaeobotanical proxy data suggests a marginally better fit with the reconstructions at lower levels of CO2.

1. INTRODUCTION

One of the ways to better understand future anthropogenic-induced climate change is to simulate past climates, using these as partial analogues for the future and allowing the testing of climate models to simulate climates very different from today (Braconnot *et al*. 2011, Tierney *et al*. 2020). Simulating past climates allows not only an interrogation of the mechanisms of past climate change (Haywood *et al*. 2020, Lunt *et al*. 2021), but if a robust comparison with available proxy data can be produced, this allows confidence in future climate change projections that are often based on models tuned to a modern climate state (Harrison *et al*. 2014, Taylor *et al*. 2011, Williams *et al*. 2020, Williams *et al*. 2021, Zhu *et al*. 2020).

It has long been known that African precipitation, and in particular that of the West African monsoon, is of vital importance to the more than one billion people in sub-Saharan Africa who survive predominantly on rain-fed agriculture and, concurrently, are highly vulnerable to extreme precipitation events causing both flooding and drought (Williams and Kniveton 2011). However, a lack of weather and climate data across much of the continent has resulted in a high level of uncertainty concerning both present day and future climate trends (Salerno *et al*. 2019), and although it is expected that both average temperature and precipitation will increase across Africa along with the rest of the world (IPCC 2021), regional variation is particularly high across Africa.

Due to their particular relevance to African monsoon precipitation, two Quaternary time periods have recently been investigated by Williams *et al*. (2020) under the Palaeoclimate Modelling Intercomparison Project (PMIP, Braconnot *et al*. 2007), now in its 4th phase and itself under the umbrella of the Coupled Model Intercomparison Project, now in its 6th phase (CMIP6, Eyring *et al*. 2016). These time periods are the mid-Holocene (6000 years ago, 6 ka) and Last Interglacial (127 ka). However, excess warmth and enhancement of Northern Hemisphere monsoons during these periods is caused primarily by changes to the orbital configuration of Earth, rather than elevated greenhouse gases (Kageyama *et al*. 2018). To investigate substantial greenhouse gas-induced warming, and its result on monsoon systems such as across Africa, periods further back in time are needed, and two such candidates in the context of PMIP are the mid-Pliocene (~3 million years ago, 3 Ma) and the early Eocene (~56.05-47.8 Ma, hereafter referred to as the Eocene). However, with CO_2 levels ranging from 316-420 ppmv during the mid-Pliocene (Martínez-Botí *et al*. 2015), this is more similar to modern levels rather than being a suitable analogue for future projections by the end of the 21st century; using the previous RCP 8.5 scenario, this could be over 1000 ppmv (IPCC 2013). The Eocene, with CO_2 levels ranging between 1200-2500 ppmv (Anagnostou *et al*. 2016, Anagnostou *et al*. 2020, Lunt *et al*. 2021), is comparable to the current future projections, and in particular for the extended high-emissions scenarios such as in the year 2300 under SSP5-8.5 (Arias *et al*. 2021). As a result of this high CO_2, the early Eocene was a period characterised by temperatures ~5°C higher than

today in the tropics (e.g., Inglis *et al*,.2020 Pearson *et al*. 2007), and much greater polar amplification with temperatures reaching ~20°C warmer than today at terrestrial high latitudes (e.g. Huber and Caballero 2011, Naafs *et al*. 2018, van Dijk *et al*. 2020).

Despite being a partial analogue for future climate change, until the last few years climate model simulations of high CO_2 periods such as the Eocene have not been evaluated within a consistent framework (Lunt *et al*. 2017); the closest to this was an informal model-data comparison, considering four climate models, known as the Eocene Model Intercomparison Project (EoMIP), undertaken by Lunt *et al*. (2012). This work focused on temperature-based metrics, however another study by Carmichael *et al*. (2016) used the same EoMIP ensemble to look at the hydrological cycle and hydroclimate changes in response to the elevated CO_2 levels in the Eocene. The results focusing specifically on Africa are discussed in more detail below but, globally, when compared to proxy data it was found that the models generally underestimated precipitation over high latitudes, and those models showing the most warming in these regions gave the best match to the data (Carmichael *et al*. 2016). Concerning the impact of elevated CO_2, it was found that all Eocene simulations showed a more intense hydrological cycle (relative to the pre-industrial era, hereafter PI), with enhanced global precipitation and evaporation, and that this was generally directly related to the elevated temperatures resulting from higher CO_2 (Carmichael *et al*. 2016). At any given level of CO_2, global precipitation changes varied widely between models, and certain regions (such as tropical Africa, discussed further below) were found to be sensitive to which model was assessed (Carmichael *et al*. 2016).

However, a disadvantage (albeit unavoidable) to EoMIP was that there was no consistent framework to the models' experimental design; each used different boundary conditions (e.g. palaeogeography) and different levels of CO_2 (Lunt *et al*. 2012). To resolve this problem, therefore, more recently the Deep Time Model Intercomparison Project (DeepMIP) was envisaged and conducted, using CMIP3 and CMIP5 models as well as some of the most recent state-of-the-art CMIP6-class models (Lunt *et al*. 2017). The large-scale features coming out of the simulations are discussed in Lunt *et al*. (2021), with several conclusions being drawn. Firstly, boundary conditions other than CO_2, discussed in Section 2.1, contributed between 3-5°C of the global mean Eocene warming, relative to the PI (Lunt *et al*. 2021). Secondly, the DeepMIP simulations showed less of a temperature spread than the models in EoMIP, and an increase in climate sensitivity (Lunt *et al*. 2021). Lastly, when compared to proxy SST data, most models reproduced the large-scale spatial patterns of the reconstructions but still struggled at the regional scale, such as in the south-west Pacific (Lunt *et al*. 2021).

Similar to Lunt *et al*. (2012), Lunt *et al*. (2021) only focused on temperature and CO_2-based metrics. The majority of recent studies looking at Eocene hydroclimate have focused on reconstructing evidence for the Asian monsoon (e.g. Farnsworth *et al*. 2019, Ma *et al*. 2019, Quan *et al*. 2012, Xie *et*

al. 2019). There are very few studies, and in particular modelling studies, focusing on Africa. The aforementioned study by Carmichael *et al*. (2016) using the EoMIP ensemble found that tropical Africa was particularly sensitive to the model in question, and that the models varied in skill (when reproducing precipitation, relative to observations) in regions of relatively low precipitation such as over northern Africa's Sahel region. Moreover, although some models showed similar PI precipitation over tropical Africa, under Eocene conditions they were quite different (Carmichael *et al*. 2016). It should be noted, however, that this study did not actually include any early Eocene mean annual precipitation (MAP) reconstructions from Africa, only some Lutetian samples. More recently, Carmichael *et al*. (2018) ran several CO_2 simulations using just the UK Met Office Hadley Centre model HadCM3L, finding an increase in both the size and frequency of extreme precipitation events over equatorial and East Africa. Although MAP changes were relatively small, extreme rainfall increased by up to 70% over parts of tropical Africa, with summer precipitation events dominating the regime over southern Africa (Carmichael *et al*. 2018). Another example of Eocene African work is that of Liu *et al*. (2019), who looked at the Asian, African and Australian monsoons across five different time periods and found that the African monsoon existed as early as the mid-Paleocene. Keery *et al*. (2018) found the variability of the Asian and African monsoons during the Eocene was predominantly accounted for by orbital configuration changes such as the precession and obliquity; in DeepMIP, however, these were kept at PI values and so, here, the impact on the African monsoon will only be down to the CO_2 or the other boundary condition changes.

In this paper four main questions are addressed:

1) How well do the DeepMIP models' PI simulations reproduce modern observations of the African monsoon?
2) What is the impact of CO_2 and other Eocene boundary conditions on the African monsoon in the DeepMIP models' Eocene simulations?
3) What are the physical mechanisms behind this precipitation response?
4) How do the DeepMIP models' Eocene simulations compare with proxy data of the African monsoon?

Section 2 of this paper briefly describes the experimental design followed by the DeepMIP models, gives a brief introduction to the models themselves, and describes the observational and proxy data used for comparative purposes. Section 3 presents the results, addressing each of the above questions. Section 4 summarises and concludes.

2. EXPERIMENT DESIGN, MODELS, AND PROXY DATA

2.1. Experiment design

The full experimental design, which all DeepMIP modelling groups were required to follow as closely as possible, is detailed extensively in Lunt *et al*. (2017) and so will only be briefly outlined here. In addition to the various CO_2 experiments, all modelling groups were required to carry out a PI simulation for comparison purposes, which was to be as close as possible to the CMIP6 standard *piControl* simulation (Eyring *et al*. 2016).

For the Eocene simulations, a number of boundary conditions needed to be changed, the key ones for the African region of which are shown in fig_ancils.

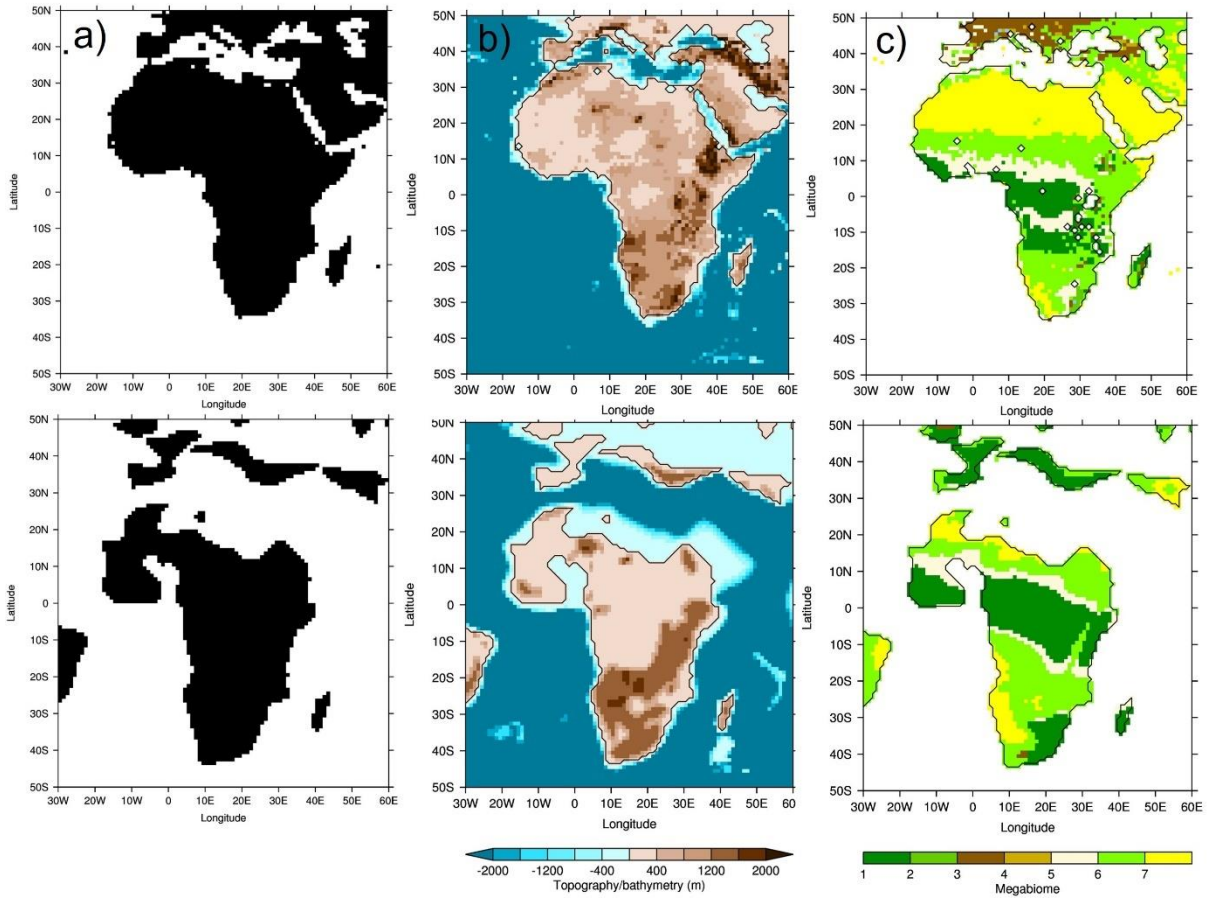

Figure 1 – Main boundary conditions changed in DeepMIP simulations, where top row = PI and bottom row = Eocene: a) Land sea mask; b) Topography/bathymetry; c) Vegetation, expressed as megabiomes according to Harrison and Prentice 2003 (where 1 = Tropical, 2 = Warm-temperate, 3 = Temperate, 4 = Boreal, 5 = Savanna, 6 = Grassland and 7 = Desert). The PI topography/bathymetry is taken from ETOPO5, re-gridded to 1°x1° resolution, whereas the other fields are from Herold *et al*. (2014)

Firstly, the land sea mask (LSM) was based on the palaeogeographic heights (discussed further below), with possible manual manipulation required in some models to maintain the various gateways (Lunt *et al*. 2017). The new LSM produced a geographically smaller Africa relative to the PI, with much of the present-day landmass north of 20°N being ocean in the Eocene due to the increased sea

level (Figure 1a). Secondly, the palaeogeography (including topography and bathymetry) was based on the digital reconstruction of the early Eocene from Herold *et al*. (2014), with the topography (and sub-grid scale topography) being applied as an absolute value rather than as an anomaly (Lunt *et al*. 2017). Over Africa, the most pronounced changes were over southern and eastern Africa, with generally larger areas of raised topography in the Eocene, relative to the PI (Figure 1b). This can be seen more clearly in the Supplementary Material, where the differences in topography are shown; there is clearly a large increase in elevation over western Africa where there is land in the Eocene but ocean in the PI, but apart from this (where the landmasses coincide) the largest changes are over southern and eastern Africa (Figure S1). Thirdly, concerning the land surface, vegetation and river run-off routing was also based on the dataset of Herold *et al*. (2014), using an appropriate lookup table to convert the vegetation megabiomes into whatever format was required by the model (Lunt *et al*. 2017). The Eocene vegetation was created by running the dynamic vegetation model BIOME4 (Kaplan *et al*. 2003), itself forced by Eocene atmospheric conditions from another climate model run and, as Herold *et al*. (2014) note, although the simulated vegetation compares well with reconstructions, over certain regions such as South Africa a lack of records meant validation was not possible. When compared to the PI, over Africa the new vegetation resulted in: i) a loss of the desert regions over the present-day Sahara, primarily because this is ocean in the Eocene; ii) a latitudinal expansion (relative to the PI) of tropical rainforest across central Africa; and iii) an addition of a large area of tropical rainforest over southern Africa, which is savanna or grassland in the PI (Figure 1c). However, some features remained similar in the Eocene relative to the PI, such as the region of tropical rainforest across central Africa being bordered by savannah to the north and south, and the Namib Desert (Figure 1c). The impact on precipitation of these three boundary condition changes is discussed below. Soil parameters, including soil dust fields, were given a globally constant value, and (given the lack of palaeodata) no lakes were prescribed unless dynamically predicted (Lunt *et al*. 2017). Concerning greenhouse gas concentrations, the CO_2 experiments were divided into a set of standard experiments (which all modelling groups should ideally have conducted) and a set of sensitivity experiments (which were optional). All of these were expressed as multiples of the PI simulation, typically with a CO_2 of 280 ppmv, and were as follows: 3x and 6x the PI for the standard experiments, and 1x, 1.5x, 2x, 4x and 9x the PI for the sensitivity experiments (Lunt *et al*. 2017). See Table 1 for which modelling groups conducted which experiments. All other greenhouse gases were kept as PI, the justification for which is given in Lunt *et al*. (2017). Concerning aerosols, given the rapid development of representation of aerosols in models the experimental design was flexible here and allowed modelling groups to either leave these as PI, treat aerosols interactively (if possible), prescribe aerosols from Herold *et al*. (2014), or a combination of the above (Lunt *et al*. 2017). The solar constant and astronomical parameters were kept identical to the PI, the justification for which is again given in Lunt *et al*. (2017).

Modelling group responsible	Model	Atmospheric resolution (lon x lat)	CO_2 experiments undertaken	Run length (years)	References
University of Michigan, US	CESM1.2_CAM5	2.5° x 1.89°	1x, 3x, 6x, 9x	2000	Hurrell *et al*. 2013
Polish Academy of Sciences, Poland	COSMOS-landveg_r2413	3.75° x 3.71°	1x, 3x, 4x	9500	Roeckner *et al*. 2003
Stockholm University, Sweden	GFDL_CM2.1	3.75° x 3.05°	1x, 2x, 3x, 4x, 6x	6000	Delworth *et al*. 2006
University of Bristol, UK	HadCM3B_M2.1aN	3.75° x 2.5°	1x, 2x, 3x	7800	Valdes *et al*. (2017)
University of Bristol, UK	HadCM3BL_M2.1aN	3.75° x 2.5°	1x, 2x, 3x	7800	Valdes *et al*. (2017)
National Academy of Sciences, Russia	INM-CM4-8	2° x 1.5°	6x	1050	Volodin *et al*. (2018)
Laboratoire des Sciences du Climat et de l'Environnement, France	IPSLCM5A2	3.75° x 1.89°	1.5x, 3x	4000	Sepulchre *et al*. (2020)
University of Tokyo, Japan	MIROC4m	2.8125° x 2.79°	1x, 2x, 3x	5000	Chan *et al*. (2011)
University of Bergen, Norway	NorESM1_F	2.5° x 1.89°	2x, 4x	2100	Guo *et al*. (2019)

Table 1 - Models taking part in DeepMIP, including relevant details and references

Lastly, the experimental design provided some advice on practical matters such as simulation length and output format. The simulations varied in length (see Table 1) but were all at least 1000 years in length, with the climatologies, comprising the results discussed here, being calculated over the final 100 years. At that point, all simulations should have had a global mean top-of-the-atmosphere (TOA) net radiation balance of less than 0.3 W m^{-2} (or a similar balance to that of the PI) and an SST trend of less than 0.1°C $century^{-1}$ (Lunt *et al*. 2017). All of the output, details of which are given in Lunt *et al*. (2017), were uploaded to a centralised DeepMIP database.

2.2. Models

Extensive details on each model, and how the experimental design was implemented in their simulations, are given in Lunt *et al*. (2021) and references therein and will therefore only briefly be discussed here; those aspects likely to affect monsoon precipitation (e.g. convection and land-surface schemes) will be focused upon here. In total, nine models were included in DeepMIP, although it should be noted that two of these are different configurations of the same model. See Table 1 for a list of the models, along with their atmospheric spatial resolutions and appropriate references

(particularly relating to the atmospheric component of the models and elements relating to hydroclimate, where available). In detail, these are as follows.

- CESM1.2_CAM5: The Community Earth System Model version 1.2 (CESM1.2) is comprised of the Community Atmosphere Model version 5.3 (CAM5), the Community Land Model version 4.0, the Community Ice Code version 4.0 and the Parallel Ocean Program version 2 (Hurrell *et al*. 2013). CAM5 uses the finite-volume dynamical core and physical parameterizations of deep convection (Zhang and McFarlane 1995), shallow convection and moist turbulence (Park and Bretherton 2009), and cloud microphysics (Morrison and Gettelman 2008). This version contains new physical parameterisations in the atmosphere, such as the cloud microphysics, which is critical for the simulation of the large-scale climate features of the early Eocene (Liu *et al*. 2017)
- COSMOS-landveg_r2413: For an atmospheric general circulation model, ECHAM5 (the European Centre Hamburg Model) is used (Roeckner *et al*. 2003), and this is coupled to the Max-Planck-Institute for Meteorology Ocean Model (MPIOM) (Marsland *et al*. 2003); the coupled model is described by Jungclaus *et al*. (2006). COSMOS-landveg_r2413 simulates cumulus convection using a mass flux scheme. The orography is represented in spectral domain by surface geopotential (see Stepanek and Lohmann 2012 for more details regarding model description). The land surface conditions for each biome are based on Hagemann (2002); additionally, parameters with a seasonal cycle (i.e. leaf area index and vegetation ratio) in the latitude belt of ~20°S-20°N were smoothed and an annual average for each biome was prescribed.
- GFDL_CM2.1: This uses the Geophysical Fluid Dynamics Laboratory (GFDL) CM2.1 model (Delworth *et al*. 2006), with modifications as described in Hutchinson *et al*. (2018), and comprising the Atmosphere Model 2, Land Model 2 and the Sea Ice Simulator 1, coupled to the ocean component from the modular ocean model version 5.1 (MOM5.1). The atmosphere uses a finite-volume discretisation, and a 3° latitude x 3.75° longitude resolution with 24 vertical levels, following the configuration of CM2Mc (Galbraith *et al*. 2011). Convection is parameterised by the relaxed Arakawa-Schubert scheme of Moorthi and Suarez (1992), with a lower-bound on entrainment as specified in Tokioka *et al*. (1988). Cloud microphysics are parameterised using the scheme of Rotstayn (1997), while cloud macrophysics use the parameterisation of Tiedtke (1993). Full details of the convection and cloud parameterisations are given in Delworth *et al*. (2006). Of possible relevance to the simulation of precipitation, the topography is smoothed using a three-point mean filter to allow a smoother interaction with the wind field (Lunt *et al*. 2021).

- HadCM3B_M2.1aN: This Hadley Centre Climate Model (HadCM3) version is documented extensively in Valdes *et al*. (2017). In particular, the model uses a single 'bulk' cloud model to parameterise dry as well as shallow and deep moist convection (Grant 1998). The cloud scheme uses a statistical parametrization via a probability density function over the grid-box total water content (Bushell 1998). Six short-wave and eight long-wave radiation bands are represented by the scheme of Edwards and Slingo (1996). Static fields for the nine surface types of the MOSES2.1 land surface scheme (Cox *et al*. 1999) are derived from the ten megabiomes of the DeepMIP vegetation boundary conditions (Herold *et al*. 2014) via a lookup table. The atmosphere uses a Cartesian grid with a horizontal resolution of 3.75 x 2.5° (longitude x latitude) and 19 hybrid vertical levels.
- HadCM3BL_M2.1aN: The only difference between this version of HadCM3 and the one described above is the horizontal resolution of the ocean component (Cox 1984), at 1.25° x 1.25° for HadCM3B_M2.1aN and 3.75° x 2.5° for HadCM3BL_M2.1aN, and associated diffusion parameters (Valdes *et al*. 2017). Both versions use 20 unequally spaced vertical levels in the ocean ranging between 10 and 616 m.
- INM-CM4-8: This version of the Institute of Numerical Mathematics (INM) model is described in Volodin *et al*. (2018), but the parameterisations of physical processes are the same as in the previous version, INM-CM5, and described more detail in Volodin *et al*. (2017). Parameterization of condensation and cloud formation follows Tiedtke (1993), and cloud water is a prognostic variable. Parameterization of cloud fraction follows Smagorinsky (1963); cloud fraction is a diagnostic variable, independent of the calculation of condensation, and depended on the relative humidity. Deep and shallow convection is parameterized by Bets (1986). The surface, soil and vegetation scheme follow Volodin and Lykossov (1998), with the evolution of the equations for temperature, soil water and soil ice being solved at 23 levels from the surface to 10 meters depth (Volodin *et al*. 2018). The fractional area of 13 types of potential vegetation is specified, and actual vegetation as well as LAI is calculated according to the soil water content in the root zone and soil temperature (Volodin *et al*. 2018).
- IPSLCM5A2: The IPSL-CM5A2 Earth system model from the Institut Pierre Simon Laplace (IPSL) is documented by Sepulchre *et al*. (2020), and is based on the previous generation IPSL Earth system model (IPSLCM5A, Dufresne *et al*. 2013) but with new revisions such as a re-tuning of global temperature. It comprises the LMDZ5 (Laboratoire de Météorologie Dynamique Zoom) atmosphere model, the Organising Carbon and Hydrology In Dynamic Ecosystems (ORCHIDEE) land surface and vegetation model and the Nucleus for European Modeling of the Ocean (NEMOv3.6) ocean model, which includes the LIM2 sea ice model and the Pelagic Interactions Scheme for Carbon and Ecosystem Studies (PISCESv2) biogeochemical model (Lunt *et al*. 2021). LMDZ5 runs at a horizontal resolution of 1.9° ×

2.5° (latitude × longitude) with 39 hybrid sigma-pressure levels. The LMDZ5 radiation scheme is inherited from the European Center for Medium-Range Weather Forecasts (Fouquart and Bonnel 1980, Morcrette et al. 1986), and the dynamical effects of the subgrid-scale orography are parameterized according to Lott (1999). Turbulent transport in the planetary boundary layer is treated as a vertical eddy diffusion (Laval et al. 1981), with counter-gradient correction and dry convective adjustment, and the surface boundary layer is treated according to Louis (1979). Cloud cover and cloud water content are computed using a statistical scheme (Bony and Emanuel 2001). For deep convection, the LMDZ5A version uses the "episodic mixing and buoyancy sorting" scheme originally developed by Emanuel (1991).

- MIROC4m: This version of the Model for Interdisciplinary Research on Climate (MIROC) is documented by K-1 model developers (2004) and summarized in Chan *et al*. (2011). In the atmosphere model, cumulus parameterization is based on Arakawa and Schubert (1974), with some simplifications and the cloud base mass flux is treated as a prognostic variable. Cumulus convection is suppressed when the cloud-mean ambient relative humidity is less than the critical value of 0.8. The land surface model (Minimal Advanced Treatments of Surface Interaction and Runoff, MATSIRO) is documented by Takata *et al*. (2003), where prognostic variables include canopy temperature, canopy water content, snow amount, soil moisture content and frozen soil moisture content. Fixed vegetation types are specified over ice-sheet-free. The ocean component is version 3.4 of the CCSR (Center for Climate System Research) Ocean Component Model (COCO), documented in Hasumi (2000).
- NorESM1_F: This version of the Norwegian Earth System Model (NorESM) is described in detail in Guo *et al*. (2019) and Li *et al*. (2020), and differs from the previous version (NorESM1-M) in that while it has the same atmosphere-land grid, the ocean and sea ice components use a tripolar grid (rather than the bipolar grid in NorESM1-M), resulting in a more realistic Atlantic Meridional Overturning Circulation (Lunt *et al*. 2021). NorESM1_F couples the Miami Isopycnic Coordinate Ocean Model (MICOM) and the spectral Community Atmosphere Model (CAM4) (Eaton 2010, Neale *et al*. 2008, Neale *et al*. 2013). CAM4 includes the Zhang and McFarlane (1995) deep convection scheme, the Hack (1994) shallow convection scheme, the nonlocal boundary layer scheme of Holtslag and Boville (1993) and the representation of cloud microphysics and macrophysics by Rasch and Kristjánsson (1998) and Zhang *et al*. (2003). Instead of using the undiluted convective available potential energy (CAPE) in the original deep convection scheme, the diluted CAPE through an explicit representation of entrainment has been used to close the cumulus parameterization (Neale *et al*. 2008). The convective momentum transport has also been included in the parameterization of deep convection (Richter and Rasch 2008). Additionally,

NorESM1_F adopts energy updates and energy conservation. Compared to NorESM1-M, NorESM1_F has several important improvements on how precipitation is simulated, such as improvements in seasonality, a reduced wet bias and mitigation of the common double intertropical convergence zone (ITCZ) problem (Li *et al*. 2020).

2.3. Observational and proxy data

Here the observational and proxy data are described; firstly there is a description of the modern, satellite-derived data used to assess and evaluate the PI simulations, and secondly there is a description of the Eocene proxy data used to evaluate the Eocene simulations.

2.3.1. Satellite-derived rainfall estimates from the modern period

Even in the 21st century, there is a severe lack of in-situ rain gauge data over Africa; South Africa is probably the best populated in terms of rainfall measurements, but in other countries such as Angola or Namibia rain gauge data are sparse or non-existent (e.g. Williams *et al*. 2007, Williams *et al*. 2008, Williams *et al*. 2010). The CenTrends precipitation dataset (Funk *et al*. 2015) contains measurements going back to 1900, but only for a small number of countries in East Africa. Likewise, although the Global Historical Climate Network (GHCN) database (Durre *et al*. 2008, Durre *et al*. 2010, Menne *et al*. 2012) does contain temperature measurements going back to 1861, precipitation measurements do not begin until the 1950s and are again relatively sparse in Africa. Therefore, a possible solution to the problem of data unavailability is to use satellite-derived rainfall estimates (SREs), which offer near-uniform coverage at relatively high spatial resolution from the 1980s onwards.

Several datasets of SREs currently exist, but here the Tropical Applications of Meteorology using SATellite data and ground-based observations (TAMSAT) is used. TAMSAT (version 3.1) provides daily, 10-daily, monthly and seasonal precipitation estimates over Africa at 4 km resolution, and extends from 1983 to the present-day. The data are publicly available; please see Data Availability and Maidment *et al*. (2014), Maidment *et al*. (2017) and Tarnavsky *et al*. (2014) for details. Here, TAMSAT is used as a comparative tool for evaluating the PI simulations of the DeepMIP models. A caveat here is that the models are showing precipitation simulated under PI boundary conditions, whereas TAMSAT is showing precipitation from the late 20th and early 21st century (referred to here as modern) and will therefore contain an anthropogenic signal; this, however, is unavoidable given the lack of PI precipitation observations. It is expected that the biases between comparing the models to PI precipitation versus comparing them to modern precipitation will be less than the biases between the models themselves (i.e. the inter-model spread), and indeed much less than the uncertainty associated with the Eocene reconstructions.

2.3.2. Palaeobotanical Eocene precipitation estimates

The distribution and physiognomy of land plants are sensitive to precipitation (Wright *et al*. 2017). Therefore, the taxonomic affinity and the morphology of leaf fossils can be used to generate palaeo-precipitation estimates (e.g. Utescher *et al*. 2014, Wilf *et al*. 1998). For this study, previously established Paleocene-Eocene palaeobotanical records from Africa were compiled (see Supplementary Material, Table S1). The distribution of the nearest living relatives (NLR) of these taxa was then analyzed using the bioclimatic analysis approach to find the highest probability precipitation range in which all taxa could co-occur (e.g. West *et al*. 2020, Willard *et al*. 2019).

Geodetic coordinates of occurrences were obtained for the NLR of each plant group from the Global Biodiversity Information Facility (GBIF) (see Supplementary Material, Table S2). These occurrence datasets were then filtered for uncertain, exotic and superfluous occurrences, as well as subjected to a random resampling to avoid regional overrepresentation of densely sampled areas. A climatic envelope for each plant group (see Table S2) was then generated by extracting precipitation data (mean annual precipitation (MAP), wettest month (WMP), driest month (DMP), warmest and coldest quarter precipitation (WQP and CQP, respectively) and the precipitation seasonality coefficient (PS)) using the DISMO package in R (Hijmans *et al*. 2005). A probability density function was then generated for each co-occurring plant group by testing the likelihood of the plant group occurring at 100,000 unique extant combination of MAP, WMP, DMP, PS, WQP and CQP. As shown in Equation 1, the product of probabilities (f) was calculated for each plant group (t) at each climatic combination (x), using the means (μ) and standard deviations (σ) of their modern-day bioclimatic envelope, for each climatic variable (c).

$$f(t_n) = \prod_{i=1}^{6} \frac{1}{\sqrt{2\sigma_c^2 \times \pi}} e^{x_c - \mu_c / 2\sigma_c^2}$$

Equation 1

A combined likelihood for all plant groups in the assemblage combined can then be calculated with the product of all likelihoods (n), shown in Equation 2.

$$f(z) = \prod_{i=1}^{n} t_n$$

Equation 2

The combination of MAP, WMP, DMP, PS, WQP and CQP with the highest likelihood is the value reported here as most representative for the assemblage, and the highest and lowest values of the

metrics with f(z) ≥ 5% of the maximum f(z) is represented as the uncertainty (using the 95% confidence interval).

Eleven plant assemblages from South Africa, Tanzania, South Sudan, Cameroon, Côte d'Ivoire, Ghana and Nigeria were analyzed with the bioclimatic analysis NLR method (Adeonipekun *et al*. 2012, Atta-Peters and Salami 2004, Cantrill *et al*. 2013, Chiaghanam *et al*. 2017, de Villiers 1997, Eisawi and Schrank 2008, Goha *et al*. 2016, Okeke and Umeji 2016, Salami 1984, Salard-Cheboldaeff 1979, Uzodimma 2013).

The NLR generated precipitation values were supplemented with an additional value based on leaf area analysis (LAA) derived data by Jacobs and Herendeen (2004) and Kaiser *et al*. (2006), also from Tanzania. In locations where the final results are in the same geographical location, the reconstructions were averaged. The final results of this analysis are shown in Table 2, with Eocene MAP expressed as ranges and modern MAP taken from TAMSAT.

Site name	**Latitude (°N)**	**Longitude (°E)**	**MAP (mm year^{-1})**	
			Eocene range	**Modern**
Koningsnaas, South Africa	-30.2	17.3	1318-1738	101
Shagamu, Nigeria	6.7	3.7	1148-2089	1762
Melut Basin, South Sudan	10	33	1175-1905	757
Kwakwa, Cameroon	4.5	9.1	1175-1905	2524
Mwadui, Tanzania	-3.9	33.5	813-1738	754
Tano, Ghana	4.7	-3	1514-2344	-
Nanka, Nigeria	6.12	7	1380-2291	1683
Abidjan margin, Côte d'Ivoire	5	-4.1	1660-1950	-
Okigwe, Nigeria	5.82	7.34	1175-1862	2311
Bende - Umuahia, Nigeria	5.47	7.45	1514-2291	2311
Araromi, Nigeria	7.7	3.5	1072-1738	1179
Mahenge, Tanzania	-4.79	34.26	720-800	707
Mahenge, Tanzania	-4.79	34.26	630-690	707
Mahenge, Tanzania	-4.79	34.26	737-815	707

Mahenge, Tanzania	-4.79	34.26	644-708	707
Mahenge, Tanzania	-4.79	34.26	710-790	707
Mahenge, Tanzania	-4.79	34.26	610-680	707
Mahenge, Tanzania	-4.79	34.26	610-680	707
Mahenge, Tanzania	-4.79	34.26	740-820	707

Table 2 - Locations and mean annual precipitation (MAP) from Eocene palaeobotanical records from Africa, and modern values. Eocene ranges of MAP are expressed as the 95% confidence interval for all locations except Mahenge, where ranges are expressed as +/- 1 standard deviation. Modern values of MAP taken from TAMSAT; missing values indicate ocean regions, as TAMSAT MAP is land only

3. RESULTS

Here the results of different comparisons are described: i) a model validation exercise, where the models' PI simulations are compared to modern observations (Section 3.1); ii) a simulation comparison, where precipitation from the models' Eocene simulations, at varying levels of CO_2, is compared (Section 3.2); iii) a simulation comparison, where the physical mechanisms behind the precipitation response are investigated (Section 3.3); and iv) a model-data comparison, where precipitation from the models' Eocene simulations is compared to available proxy data (Section 3.4).

3.1. DeepMIP models' preindustrial simulations versus modern observations

Here the focus is on mean precipitation differences between the various DeepMIP PI simulations (including the multi-model ensemble mean, MME) and precipitation observations from TAMSAT (see Section 2.3.1). Precipitation anomalies (PI simulations - TAMSAT) during the core West African monsoon period (June-August, JJA) are shown in Figure 2, where the models have been ordered according to the root mean square error (RMSE), relative to TAMSAT. Two observations are noteworthy. Firstly, the MME is showing by far the closest agreement to TAMSAT, with a much lower RMSE (by ~10 mm month^{-1} less than even the next lowest individual model), highlighting the importance of using the MME to counterbalance individual models' biases (whether they be under or overestimating). The MME will therefore subsequently be used when discussing the various Eocene simulations. Secondly, there appears to be a divide between: a) models such as IPSLCM5A2, INM-CM4-8 and COSMOS-landveg_r2413 that are underestimating African precipitation (i.e. are showing drier conditions across West Africa at ~10°N), which have relatively low RMS error compared with TAMSAT; and b) models such as HadCM3BL_M2.1aN, MIROC4m and GFDL_CM2.1 that are overestimating African precipitation, which have relatively high RMS error compared with

TAMSAT. For example, the model with the least agreement (GFDL_CM2.1, RMSE = 70.6 mm month^{-1}) is overestimating precipitation over West Africa by more than 100 mm month^{-1}.

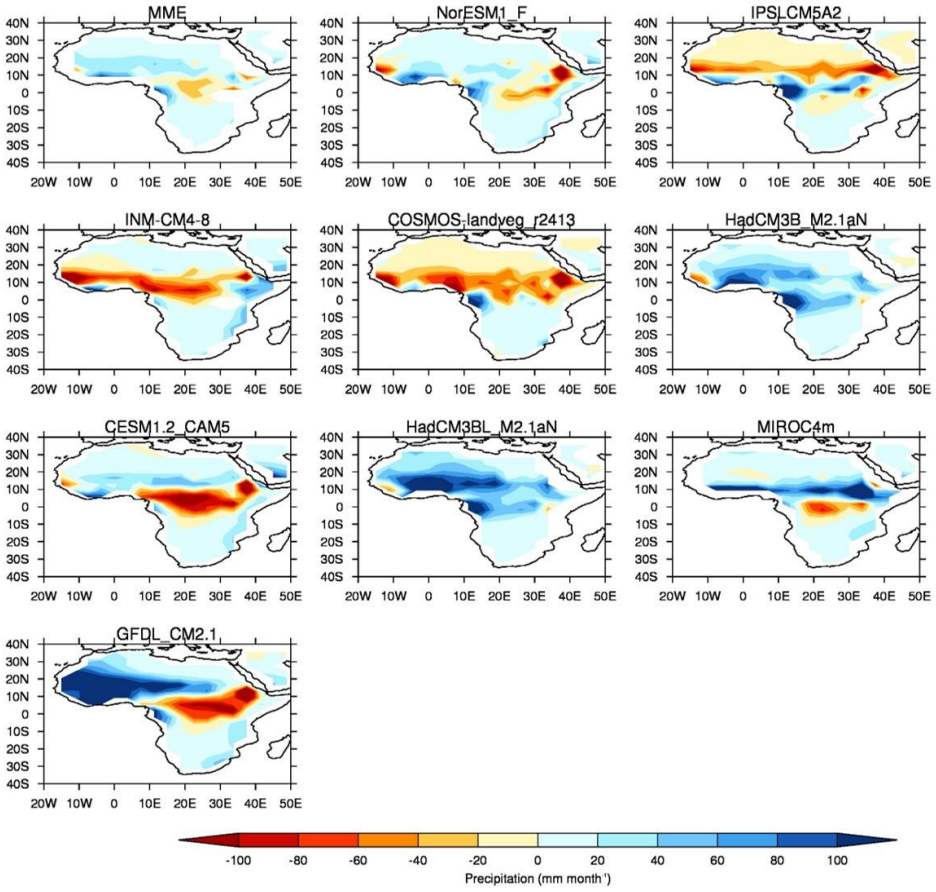

	RMSE
MME	23.90
NorESM1_F	32.96
IPSLCM5A2	42.14
INM-CM4-8	42.21
COSMOS-landveg_r2413	43.26
COSMOS-landveg_r2413 (TO)	43.37
HadCM3B_M2.1aN	43.41
CESM1.2_CAM5	43.84
HadCM3BL_M2.1aN	53.91
MIROC4m	56.69
GFDL_CM2.1	70.64

Figure 2 - JJA precipitation climatology differences (PI simulations - TAMSAT), re-gridded to lowest common spatial resolution (that of COSMOS-landveg_r2413) and ordered according to Root Mean Squared Error (RMSE, in mm month^{-1}, see insert). RMSE calculated over 20°W-50°E, 40°N-40°S, land points only

Concerning the seasonal and latitudinal distribution of African precipitation, Figure 3 shows the annual cycle of West African (defined here as land points only encompassing 20°W-15°E, 0-20°N) precipitation and the zonal mean of JJA West African precipitation (Figure 3a and b, respectively). Outside of the JJA monsoon season, the majority of models are overestimating precipitation throughout the year (Figure 3a), with the model closest to TAMSAT (in terms of the seasonal cycle i.e. precipitation timings) being CESM1.2_CAM5, although even this model overestimates precipitation during the first half of the year. When averaged over this region, only one model (INM-CM4-8) underestimates precipitation throughout the year, but is nevertheless closer to TAMSAT than those which overestimate, in agreement with that discussed above and shown in Figure 2. One model (GFDL_CM2.1) greatly overestimates precipitation especially during the monsoon season, and others (such as INM-CM4-8) underestimate precipitation during the monsoon season and therefore do not correctly reproduce the strong seasonality (i.e. the precipitation curve is flatter); for example, the

490 difference between the wettest and driest month in this model is 136 mm month^{-1}, whereas it is 161
491 mm month^{-1} in TAMSAT and 181 mm month^{-1} in the MME (Figure 3a). The MME also
492 overestimates precipitation throughout the year but is nevertheless closer to TAMSAT in terms of
493 seasonality than many of the wetter models (Figure 3a). Latitudinally, most models are showing a
494 much wider (in terms of latitudinal extent) rain belt relative to TAMSAT, with GFDL_CM2.1 and the
495 HadCM3 family in particular not reproducing the observed rapid drop-off in precipitation either near
496 the Equator or north of 15°N (Figure 3b). In part due to some drier models approaching the Equator
497 (such as CESM1.2_CAM5 and INM-CM4-8), the MME is showing a similar latitudinal extent of
498 precipitation compared to TAMSAT, and while it is still too wet at low latitudes it does correctly drop
499 off north of 15°N (Figure 3b).
500

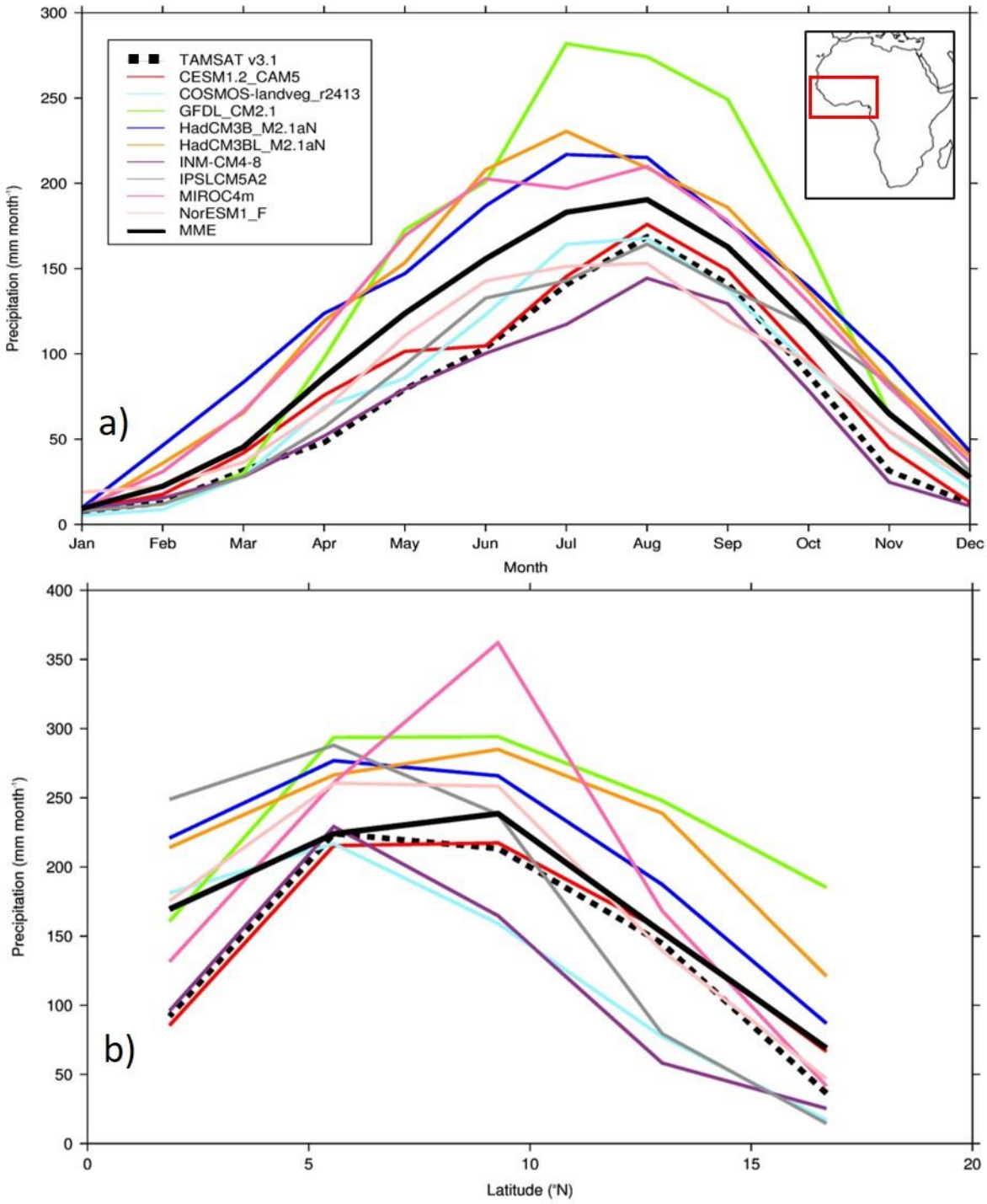

Figure 3 - Precipitation climatology from TAMSAT and PI simulations, averaged over West Africa (20°W-15°E, 0-20°N - land points only): a) Mean seasonal cycle, at each model's individual spatial resolution; b) Zonal mean of JJA precipitation, re-gridded to lowest common spatial resolution

3.2. DeepMIP models' Eocene simulations relative to preindustrial simulations and each other

Here the focus is on mean precipitation differences between various DeepMIP Eocene CO_2 sensitivity experiments, in which all boundary conditions other than CO_2 were kept identical. The focus is not

only on the precipitation response to varying CO_2 concentrations relative to the PI simulations, but also from each CO_2 experiment individually (relative to each other). Precipitation anomalies of all the CO_2 experiments versus PI are firstly briefly presented (Section 3.2.1), and then the experiment results are divided into a non-CO_2 component (i.e. the impact of the other boundary condition changes, Section 3.2.2) and a CO_2 component (Section 3.2.3).

3.2.1. All CO_2 experiments versus preindustrial

The precipitation anomalies (Eocene - PI), for each CO_2 experiment and for each model during JJA are shown in Figure 4. This is only briefly presented, because the combination of a palaeogeographic forcing and a CO_2 forcing makes interpretation difficult; this is why the results are broken down into a non-CO_2 component and CO_2 component below. It should be noted that when the MME is discussed below (see Sections 3.2.2 and 3.2.3), only models that participated in the particular experiment are included.

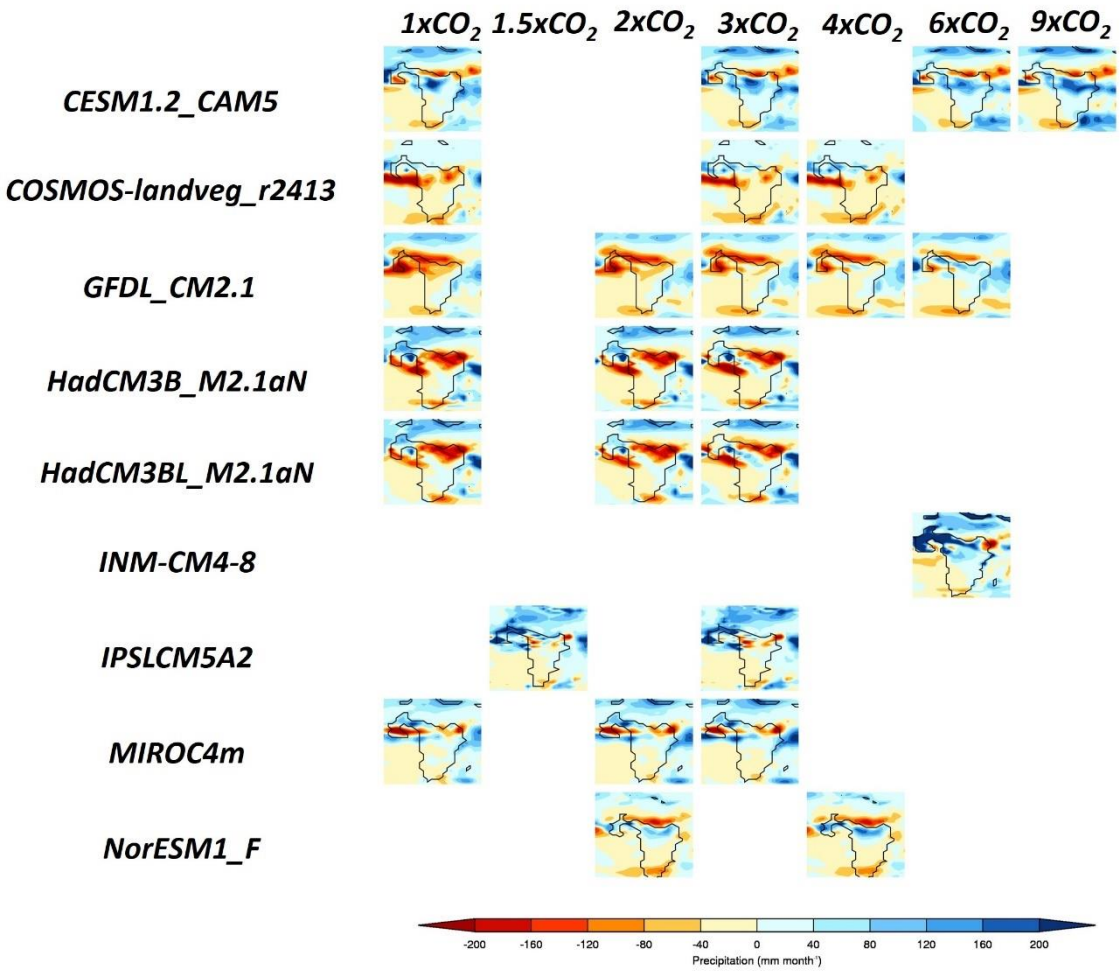

Figure 4 - JJA precipitation climatology differences (Eocene - PI), for each CO_2 simulation from each model

There is no clear linear trend in either wetting or drying across Eocene Africa as the CO_2 concentrations increase (Figure 4). Although many models show drying (relative to the PI) of up to ~180 mm month^{-1} across northern and western Africa in the 1x, 2x and 3x experiments, this gradually disappears as higher CO_2 concentrations are applied, with some models showing precipitation increases of over 200 mm month^{-1} (Figure 4). Some models disagree regardless of experiment, such as GFDL_CM2.1 which shows drying over northern Africa in all CO_2 experiments contrasting with IPSLCM5A2 which shows wetting over northern Africa in all CO_2 experiments. Further south, none of the models in any of the experiments are showing a large precipitation response. In very general terms, however, at the lower levels of CO_2 concentrations (i.e. up to 4x) the majority of models are showing the same region of drying over northern and western Africa.

3.2.2. 1x CO_2 experiment versus preindustrial: impact of non-CO2 boundary conditions

The 1x CO_2 experiment versus PI is of particular interest, because this shows the impact of the other boundary conditions rather than that from CO_2 concentrations. When CO_2 concentrations are kept as PI (as in the 1x experiment), the boundary conditions (see Section 2.1) likely to have the largest impact on regional precipitation are the LSM, topography and vegetation (see Figure 1). Although land ice changes, the largest of which during the Eocene were over the Antarctic Ice Sheet (AIS), do cause a precipitation response (e.g. Kennedy-Asser *et al*. 2019), this is thought to be a mainly local signal and further afield, such as over northern and western Africa during JJA, there is little or no precipitation change when the AIS is either imposed or removed (Kennedy-Asser, pers. comm.).

The MME precipitation anomaly for this experiment is shown in Figure 5a; it should be noted that, although six models conducted this experiment (CESM1.2_CAM5, COSMOS-landveg_r2413, GFDL_CM2.1, HadCM3B_M2.1aN, HadCM3BL_M2.1aN and MIROC4m), only the latter four are included here in the MME, to be consistent with the analysis of the CO_2 component (Section 3.2.3). From the available DeepMIP results, it is impossible to disentangle the boundary conditions and ascertain which is dominant in causing the precipitation response; in an ideal world, sensitivity experiments would be conducted to introduce each boundary condition individually, but this is not possible with the results currently available on the DeepMIP database. Nevertheless, based on the results it is possible to theorise which of these boundary conditions might be causing this MME precipitation response. The largest precipitation changes relative to the PI are a small increase in precipitation to the north of Eocene Africa and in the western Indian Ocean, and a decrease in precipitation over western and northern equatorial Eocene Africa (Figure 5a). It is likely that the northern increases are caused by the change in the LSM (Figure 1a) as this region comprises the preindustrial (and modern) Sahara but is ocean in the Eocene and therefore would have been a much greater moisture source. Likewise, the increase over the western Indian Ocean is likely because preindustrial Africa extends much further East than during the Eocene, again giving much less of a

moisture source during the PI (Figure 1a). Moreover, an examination of SST from the Eocene and PI simulations (from each individual model and the MME) shows that these exposed regions of ocean are characterised by warmer SSTs in the Eocene; for example, in the Indian Ocean absolute values are up to 32°C in the Eocene MME compared to up to 28°C in the PI MME, thereby providing a greater source of evaporation during the Eocene see (see Supplementary Material, Figure S2). Concerning the drying over equatorial Eocene Africa, this is likely less related to the LSM (because the region was land during both time periods), and more likely related to the change in vegetation (Figure 1c). In these regions, at approximately 10°N, what is tropical rainforest during the PI is rather a mixture of savanna, grassland and desert during the Eocene (Figure 1c) and would therefore likely explain the reduction in precipitation because of the reduced evapotranspiration. Finally, although there is a large increase in orographic heights (of over 1000 m) over southern Africa during the Eocene (Figure 1b and Figure S1 in the Supplementary Material), this does not appear to be having a large impact on the West African monsoon, with minimal precipitation differences further south (Figure 5a).

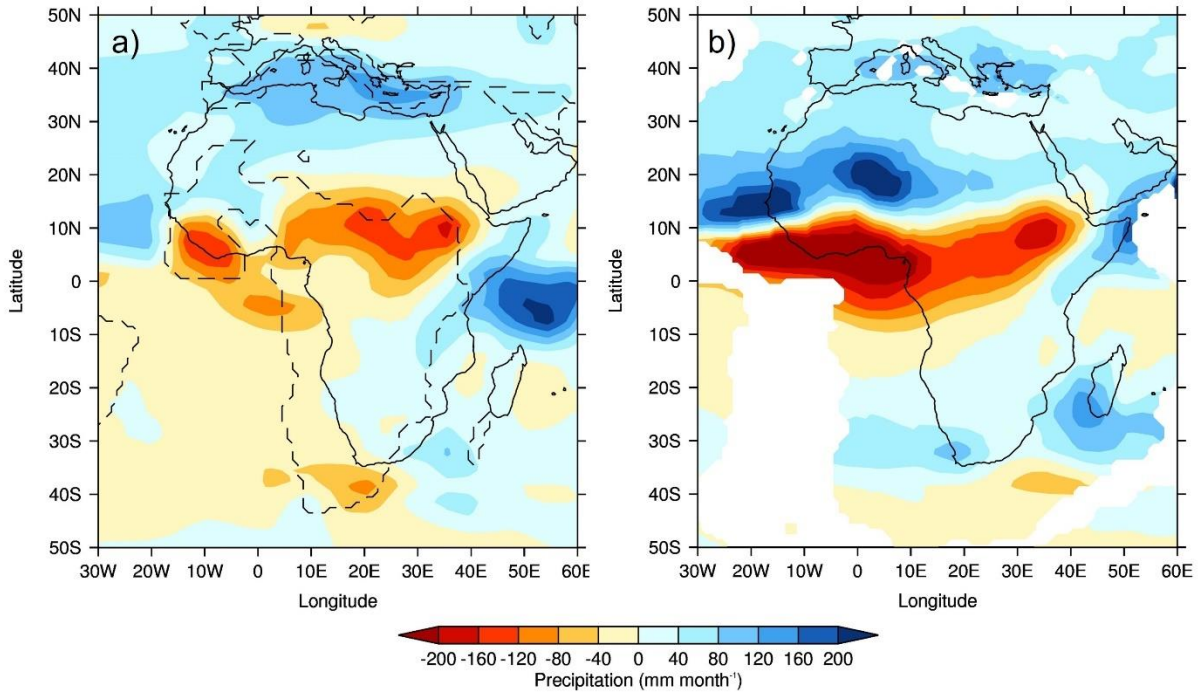

Figure 5 – JJA precipitation multi-model ensemble mean (MME) climatology differences (Eocene - PI) for the 1x CO_2 experiment (comprising the four models that conducted this experiment, in addition to the others considered here: GFDL_CM2.1, HadCM3B_M2.1aN, HadCM3BL_M2.1aN and MIROC4m): a) Original (i.e. unrotated) differences; b) Rotated differences i.e. Eocene precipitation rotated forward to where it is in the PI. Note that in a), solid lines show the PI mask and dashed lines show the Eocene mask

However, a caveat of the above analysis is that, because of the plate rotation differences during the Eocene, Figure 5a is showing precipitation anomalies that may simply be due to differing geographical locations, rather than any change to the climate state. Therefore, Figure 5b shows the same results, but this time with the Eocene precipitation rotated forwards (based on the rotations

supplied in the Herold *et al*. 2014 Supplementary Material) to where it is in the PI. However, despite these rotational differences, the overall picture remains the same (i.e. increases in precipitation over northern Africa and a decrease in precipitation over western and equatorial Africa) but much more pronounced (Figure 5b). The increases and decreases in precipitation exceed 200 mm month^{-1} in some places, suggesting a northward displacement of the Atlantic ITCZ; this difference between the Eocene and the PI is in contrast to when the Eocene CO_2 experiments are compared with each other, to assess the impact of increasing CO_2 (discussed further below in Section 3.2.3 and Section 4).

3.2.3. Lower and higher CO_2 experiments: impact of CO_2

To investigate the impact of increasing CO_2 on precipitation, when all other boundary conditions are constant, the experiments have been divided into two samples, each containing a different number of models going into the MME: i) "lower-level CO_2", namely the 1x, 2x and 3x experiments, comprising four models (GFDL_CM2.1, HadCM3B_M2.1aN, HadCM3BL_M2.1aN and MIROC4m); and ii) "higher-level CO_2", namely the 3x and 6x experiments, comprising two models (CESM1.2_CAM5 and GFDL_CM2.1); see Table 1. Note that the MMEs for the two 3x experiments are slightly different because they contain a different number of models. Here, both absolute precipitation values and anomalies are shown, where the anomalies are of a certain CO_2 experiment versus another CO_2 experiment, rather than Eocene versus PI.

The MME absolute precipitation and anomalies for the lower-level sample of CO_2 experiments, are shown in Figure 6a. When the absolute values are considered (Figure 6a, top row), all experiments show regions of precipitation maxima over the equatorial Atlantic (north of the Equator) and West Africa. Over the same West African region as described above (20°W-15°E, 0-20°N, land points only), mean JJA precipitation is 192 mm month^{-1}, 201 mm month^{-1} and 207 mm month^{-1} for the 1x, 2x and 3x experiments, respectively, implying a small increase as CO_2 increases. This becomes more evident when the anomalies are considered (Figure 6a, second row). If the 1x and 2x experiments are compared, the largest change is over the equatorial Atlantic, with a small increase in precipitation of up to 50 mm month^{-1} over the Equator and a decrease of over 50 mm month^{-1} further north, suggesting a southward displacement of the Atlantic ITCZ. Precipitation is also increased over western Africa. The same pattern is evident when the 1x and 3x experiments are compared, but more pronounced, with both the increases and decreases approaching 100 mm month^{-1} in their respective areas.

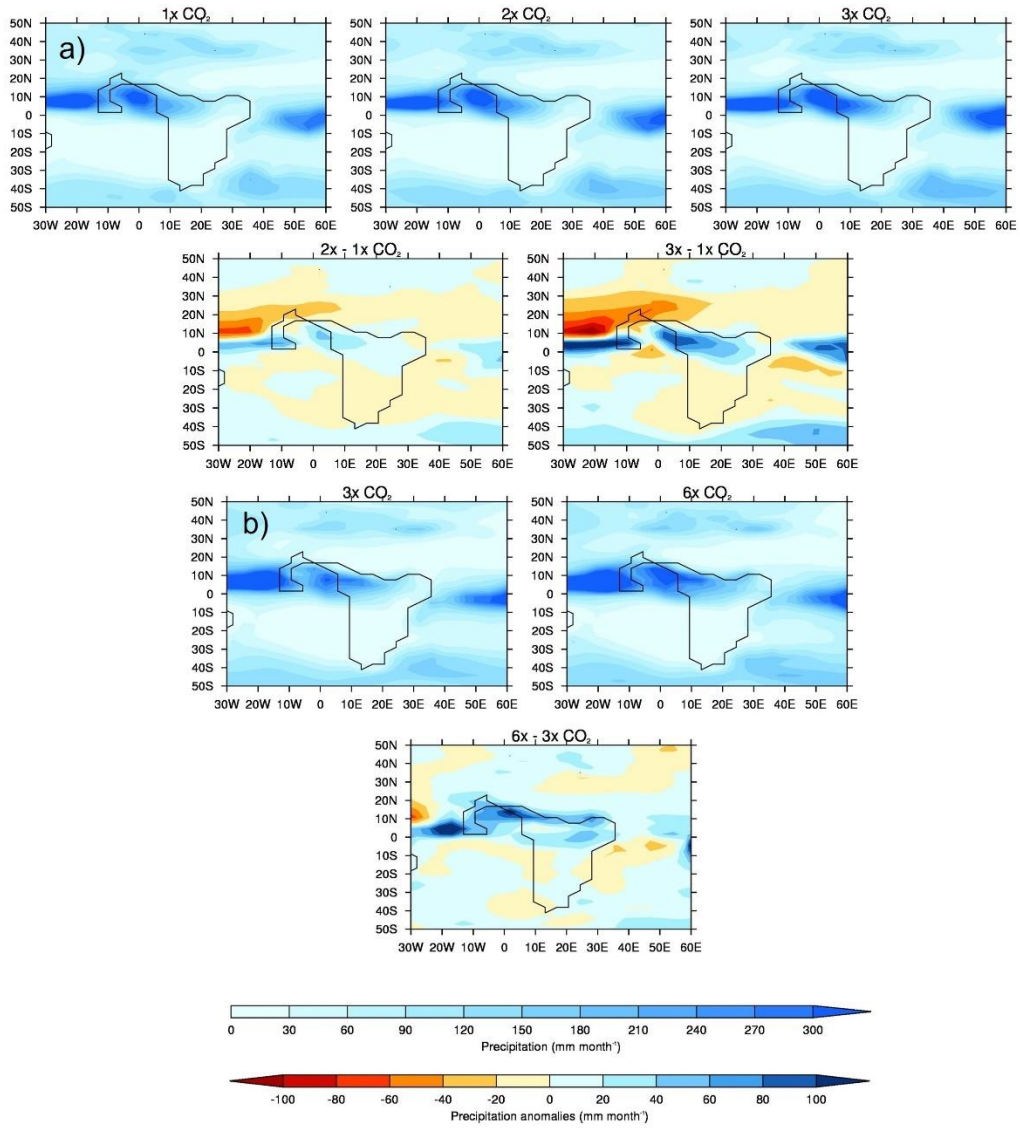

Figure 6 – JJA precipitation multi-model ensemble mean (MME) climatology absolutes and anomalies for the 1x, 2x, 3x and 6x CO_2 experiments, using both samples: a) Lower-level sample of CO_2 experiments (comprising the four models that conducted these: GFDL_CM2.1, HadCM3B_M2.1aN, HadCM3BL_M2.1aN and MIROC4m), absolutes (top row) and anomalies (second row); b) Higher-level sample of CO_2 experiments (comprising the two models that conducted these: CESM1.2_CAM5 and GFDL_CM2.1), absolutes (top row) and anomalies (second row)

The MME absolute precipitation and anomalies for the higher-level sample of CO_2 experiments are shown in Figure 6b. When the absolute values are considered (Figure 6b, top row), the region of precipitation maxima in the equatorial Atlantic is larger in the 6x experiment. Over the same West African region, mean JJA precipitation is 186 mm $month^{-1}$ and 232 mm $month^{-1}$ for the 3x and 6x experiments, respectively, implying a large mean increase as CO_2 increases, and this is further confirmed when the anomalies are considered (Figure 6b, second row). Precipitation increases of over 100 mm $month^{-1}$ are shown over the equatorial Atlantic (north of the Equator) and West Africa

635 in the 6x relative to the 3x experiment, but the large region of drying seen at the lower levels of CO_2
636 is less evident (Figure 6b, second row). This suggests that, whilst West African precipitation is still
637 (and more so here) enhanced as CO_2 rises, it is perhaps less related to Atlantic ITCZ displacement and
638 more related to an increase in south-westerly flow (discussed below).
639
640 **3.3. Physical mechanisms behind the precipitation response**
641 Here the focus is on the possible dynamic and thermodynamic mechanisms causing the observed
642 precipitation responses, again using the MME absolute values and anomalies from the aforementioned
643 lower-and higher level samples of CO_2 experiments.
644
645 The MME absolute 1.5 m surface air temperature (SAT) and anomalies for the lower- and higher-
646 level sample of CO_2 experiments are shown in Figure 7. In line with general understanding there is a
647 clear increase in absolute SAT, everywhere, as the CO_2 increases, with the largest signal (of up to
648 40°C in the 3x experiment) occurring over the main landmass of central and northern Africa (Figure
649 7a, top row). This is more obvious when the anomalies are considered, although the largest increases
650 are occurring further south (Figure 7a, second row). This is even more pronounced in the higher-level
651 sample of CO_2 experiments (Figure 7b), and in all experiments the largest increase in SAT, either
652 between the 3x and 1x experiments or the 6x and 3x the experiments, is occurring over southern
653 Africa, away from the largest precipitation changes discussed above. The Precipitation - Evaporation
654 (P-E) balance (Figure 8) is positive over West Africa in all experiments regardless of sample,
655 corresponding well with the region of increased precipitation (Figure 6), as does cloud cover which is
656 also increasing with CO_2 over these regions (not shown). Further south, over the Atlantic, the balance
657 is negative implying increased evaporation corresponding to the increased oceanic SAT. Concerning
658 low level circulation, as shown by 850 mb vector winds (Figure 9), when the anomalies are
659 considered (and in particular the 3x versus 1x), there is a small (of up to 5 ms^{-1}) increase in northerly
660 and westerly winds (i.e. clockwise flow) in the equatorial Atlantic north of the Equator (Figure 9a,
661 second row). However, in the higher-level CO_2 sample (and in particular the anomalies of 6x versus
662 3x, Figure 9b, second row), this increase in anticyclonic flow is less evident and is instead replaced by
663 a widespread area of increased southwesterly flow across most of the equatorial Atlantic and central
664 Africa. For SAT, P-E and 850 vector winds from each individual model, rather than the MME, see
665 the Supplementary Material (Figure S3a, b, and c, respectively); here, similar to Figure 4, there is no
666 obvious linear change in either P-E or low level circulation as CO_2 increases, but a clear increase in
667 SAT from all models, in line with current understanding (Figure S3a).
668

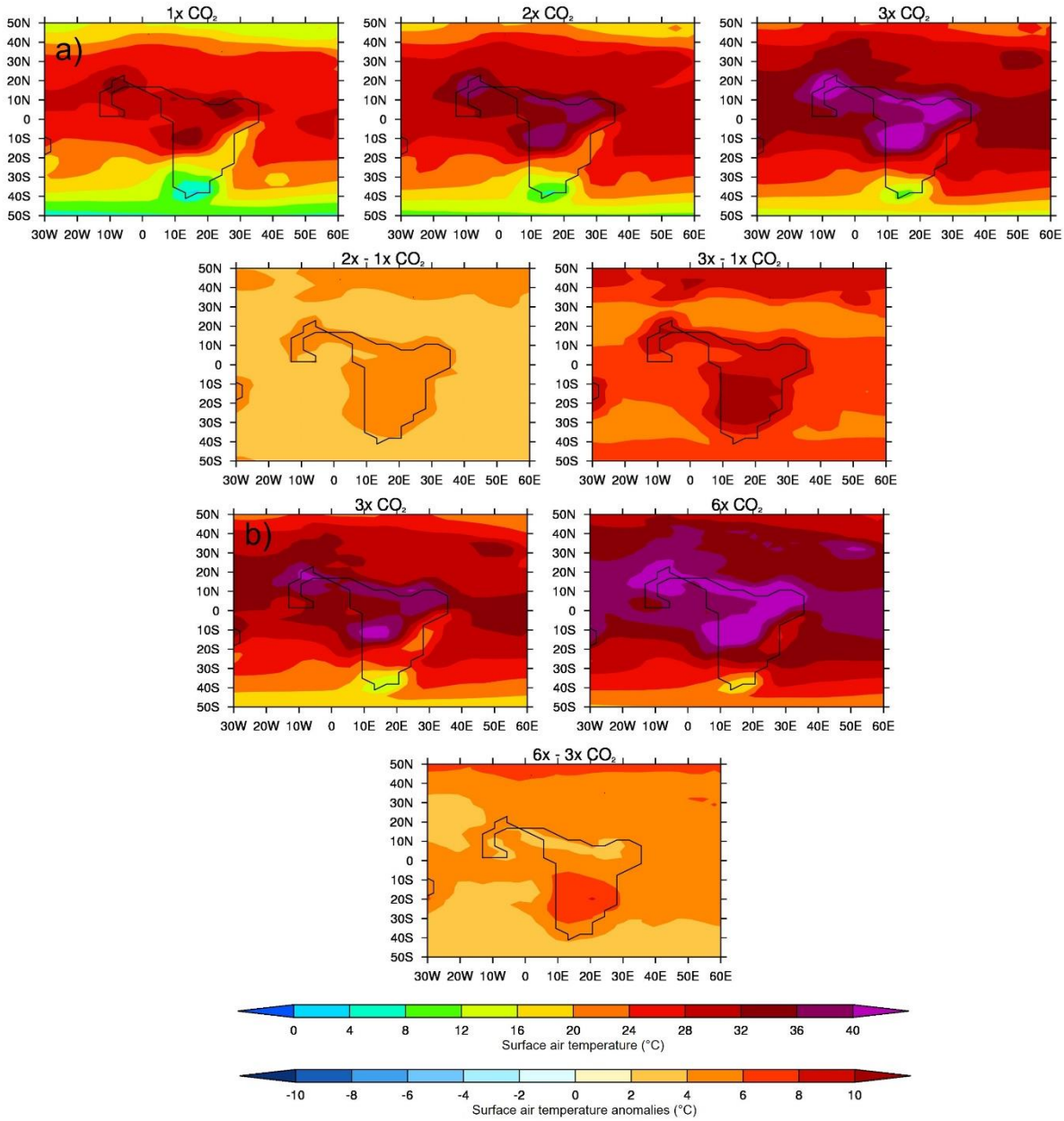

669

670 Figure 7 – Same as Figure 6 but for JJA 1.5 m surface air temperature

671

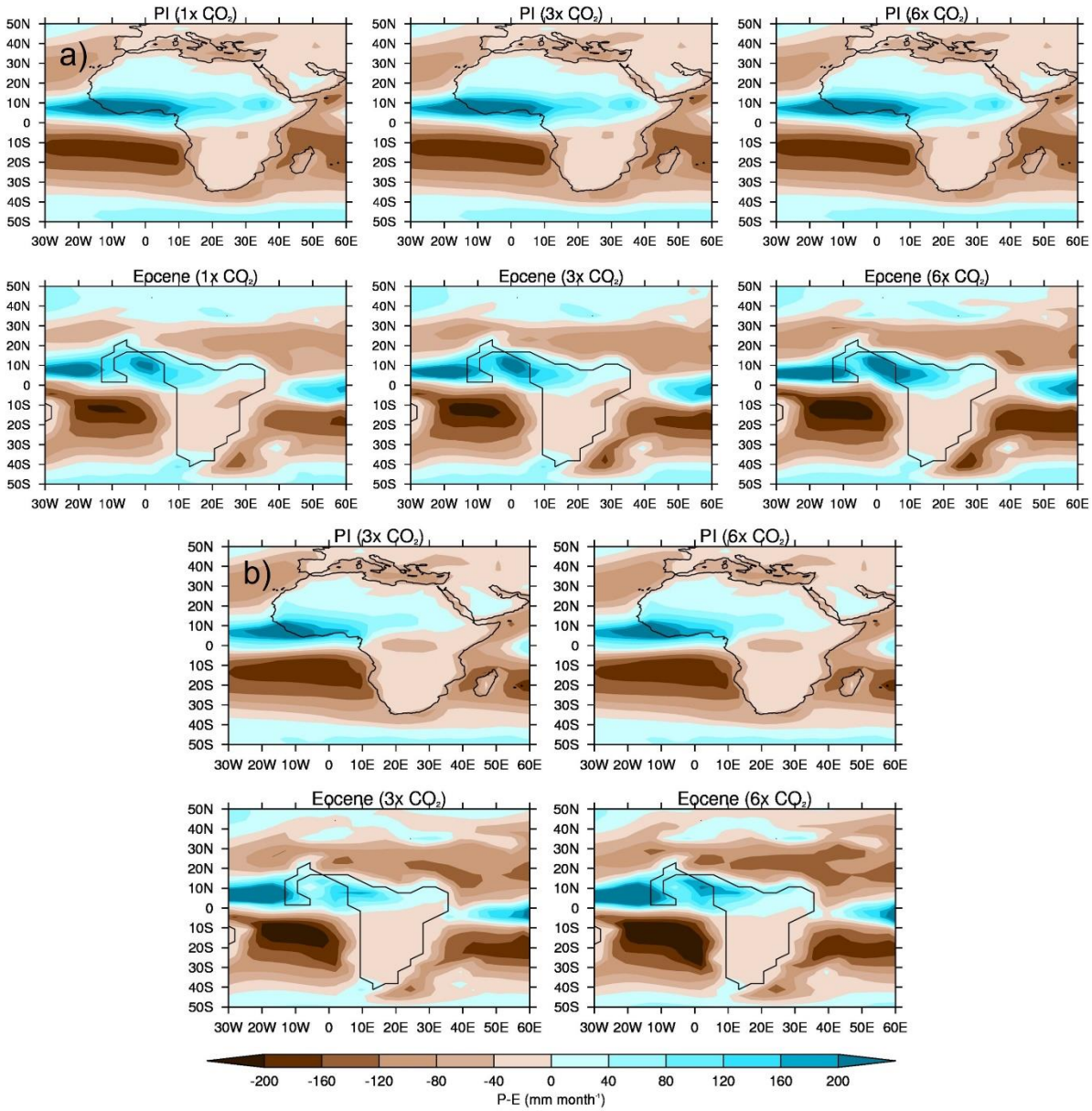

Figure 8 – JJA P-E multi-model ensemble mean (MME) climatology absolutes for the 1x, 2x, 3x and 6x CO_2 experiments, using both samples: a) Lower-level sample of CO_2 experiments (comprising the four models that conducted these: GFDL_CM2.1, HadCM3B_M2.1aN, HadCM3BL_M2.1aN and MIROC4m), PI (top row) and Eocene (bottom row); b) Higher-level sample of CO_2 experiments (comprising the two models that conducted these: CESM1.2_CAM5 and GFDL_CM2.1), PI (top row) and Eocene (bottom row). Note that the PI panels are identical in each sample because they contain the same models, but are simply replicated here for ease of comparison

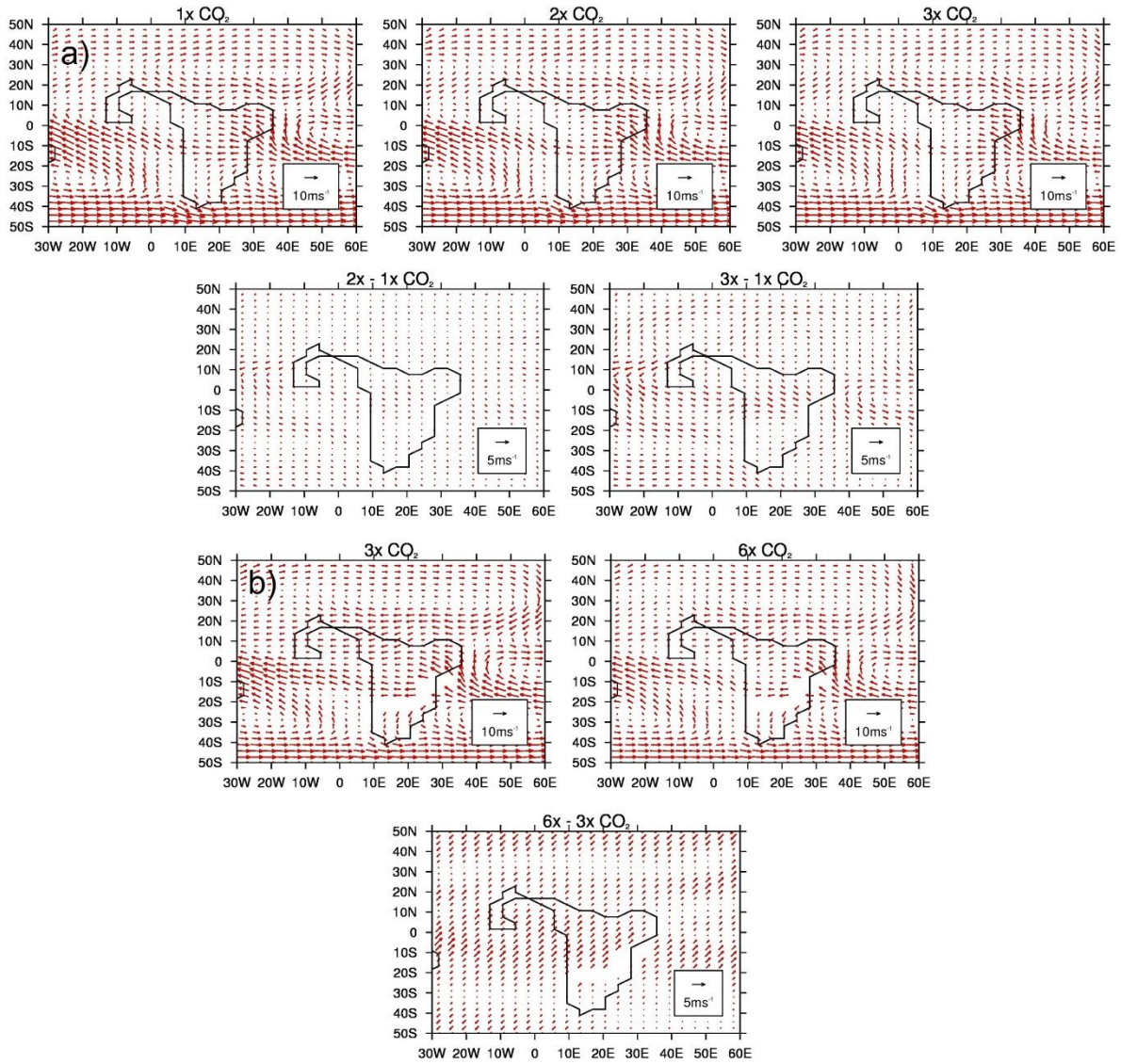

Figure 9 – Same as Figure 6 but for JJA 850 mb wind

3.4. DeepMIP models' Eocene simulations versus proxy data

In this final section, the focus is on comparing precipitation from selected DeepMIP Eocene simulations (using the MME from the same two samples as discussed above) with newly-available precipitation reconstructions (described in Section 2.3.2). Before the results are presented, however, several sources of uncertainty in the proxies and models must be noted, aside from analytical uncertainty that is expressed in the reconstructed confidence intervals. Firstly, the fossil plant assemblages analysed here have broad age constraints. Palaeofloral assemblages may capture a snapshot within those age constraints that deviated climatically from the average climatic conditions of a specific age that the model was calibrated on. In addition, fossil plant assemblages tend to preserve better in wetter climates, with drier climates lacking the water bodies needed to preserve plant fossils. Secondly, the DeepMIP models are calibrated on atmospheric CO_2 proxy reconstructions to cover the uncertainty of the entire Eocene; the lower CO_2 levels may be more

representative of the late Eocene, but that was not the purpose or interpretation when it came to deciding the experiments. Independent proxies within those ages produce widely variable atmospheric CO_2 reconstructions (e.g. Rae *et al*. 2021), with <500 ppmv from some palaeosol and stomatal reconstructions (Beerling *et al*. 2009; Hyland *et al*. 2013) to >2000 ppmv from boron isotopes and alkenone δ13C (e.g. Bijl *et al*. 2010; Anagnostou *et al*. 2020). It should be noted, however, that there is high uncertainty in these reconstructions; see Hollis *et al*. 2019 for a full discussion. For example, based on a variety of reconstructions compiled as part of the Palaeo-CO_2 project (including phytoplankton, boron proxies, leaf gas exchange, liverworts and nahcolite), atmospheric CO_2 during 55-50 Ma ranges from 500-2000 ppmv (Anagnostou *et al*. 2020, Hollis *et al*. 2019, Westerhold *et al*. 2020). Potentially, these differences in reconstructed atmospheric CO_2 reflect transient climate states (e.g. Reichgelt *et al*. 2016), but regardless, the disagreement between proxy reconstructions makes it problematic to associate a single atmospheric CO_2 level for model-data comparison (Hollis *et al*. 2019). Lastly, a major source of uncertainty is the paucity of proxy data across Africa; as mentioned above, even today there is a lack of long-term climate data over much of Africa, and the same is true for palaeofloras. This sparsity, therefore, is likely responsible for some of the results discussed below.

With these caveats in mind, MME MAP at each of the individual locations is shown in Figure 10, ordered according to the reconstructions' values, including uncertainty estimates for the reconstructions (as measured by +/- 1 standard deviation for the locations in Mahenge, Tanzania and the 95% confidence interval for the other 11 locations; see Table 2 for details). The approximate geographical locations can be seen in the Supplementary Material (Figure S4). Firstly it is worth noting that for the majority of reconstructions, uncertainty is high, with a range of up to +/- 1000 mm yr^{-1} at some of the locations such as Mwadui, Tanzania (Figure 10). Secondly, whether or not the CO_2 experiments over- or underestimate MAP appears to depend heavily on geographical location, with none of the CO_2 experiments (not even the 6x experiment) reproducing the precipitation amounts of the proxy reconstructions in some locations, such as Koningsnaas, South Africa, Okigwe, Nigeria or Tano, Ghana (Figure 10). Elsewhere, the simulations lie within the uncertainty range of the reconstructions (such as Sagamu or Bende-Umuahia, both in Nigeria), and yet in other places (such as across Kwakwa, Cameroon, and all of the locations at Mahenge, Tanzania) all of the simulations are too wet, by between ~760-1040 mm $year^{-1}$ depending on location and CO_2 experiment (Figure 10).

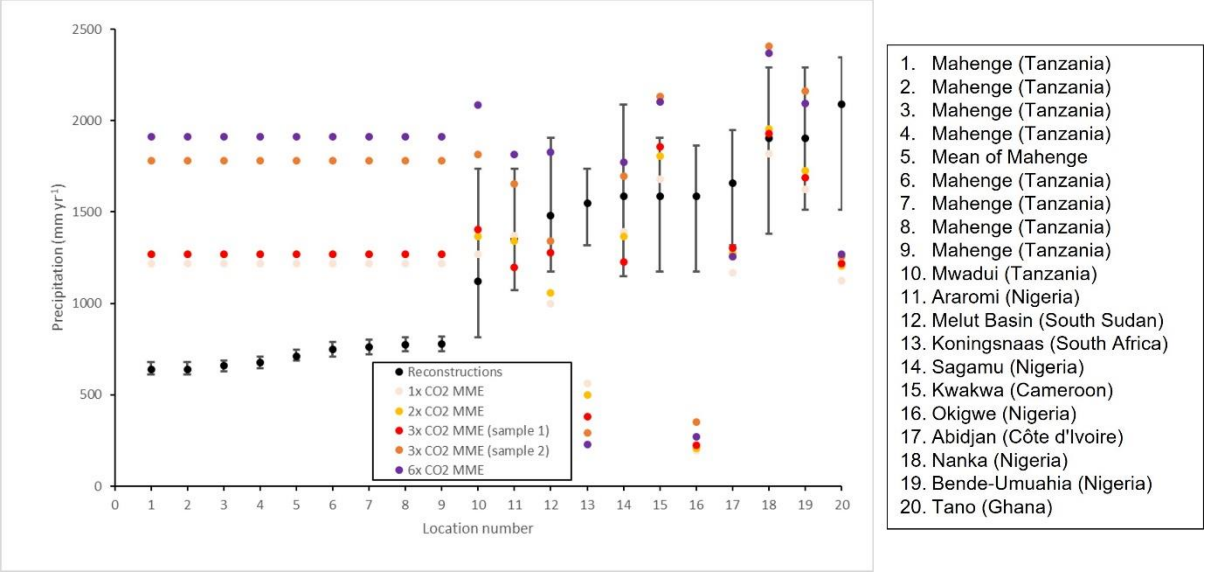

Figure 10 – Annual mean precipitation from reconstructions (black) and CO_2 experiments multi-model ensemble mean (MME, colours) at each individual location. Uncertainty in reconstructions is measured by 95% confidence interval for all sites except Mahenge, where they show +/- 1 standard deviation. Locations have been ordered according to the reconstructions' values, lowest to highest. Note that locations 1-4 and 6-8 are all in the same location, but from different stages during the Lutetian (~41-47 Ma), and so have been re-sampled and averaged into one overall mean (location 5)

Spatially, MME MAP is shown in Figure 11 (see Figure S5 in the Supplementary Material for each individual model), showing the uncertainty estimates as concentric circles. As already discussed, the simulations' precipitation is clearly too high or too low compared to proxy reconstructions in different parts of Africa. Qualitatively, in very general terms all of the CO_2 experiments are showing wetter conditions over Western Eocene Africa (relative to elsewhere), agreeing with Figure 10 where in many of these locations the models are either within, or at the higher end of, the reconstructions' uncertainty ranges (Figure 11). Importantly, simulated precipitation over West Africa appears to be increasing as the CO_2 concentration increases and, in particular for the 6x experiment (Figure 11e), in this region simulated precipitation exceeds even the upper range of uncertainty of the reconstructions.

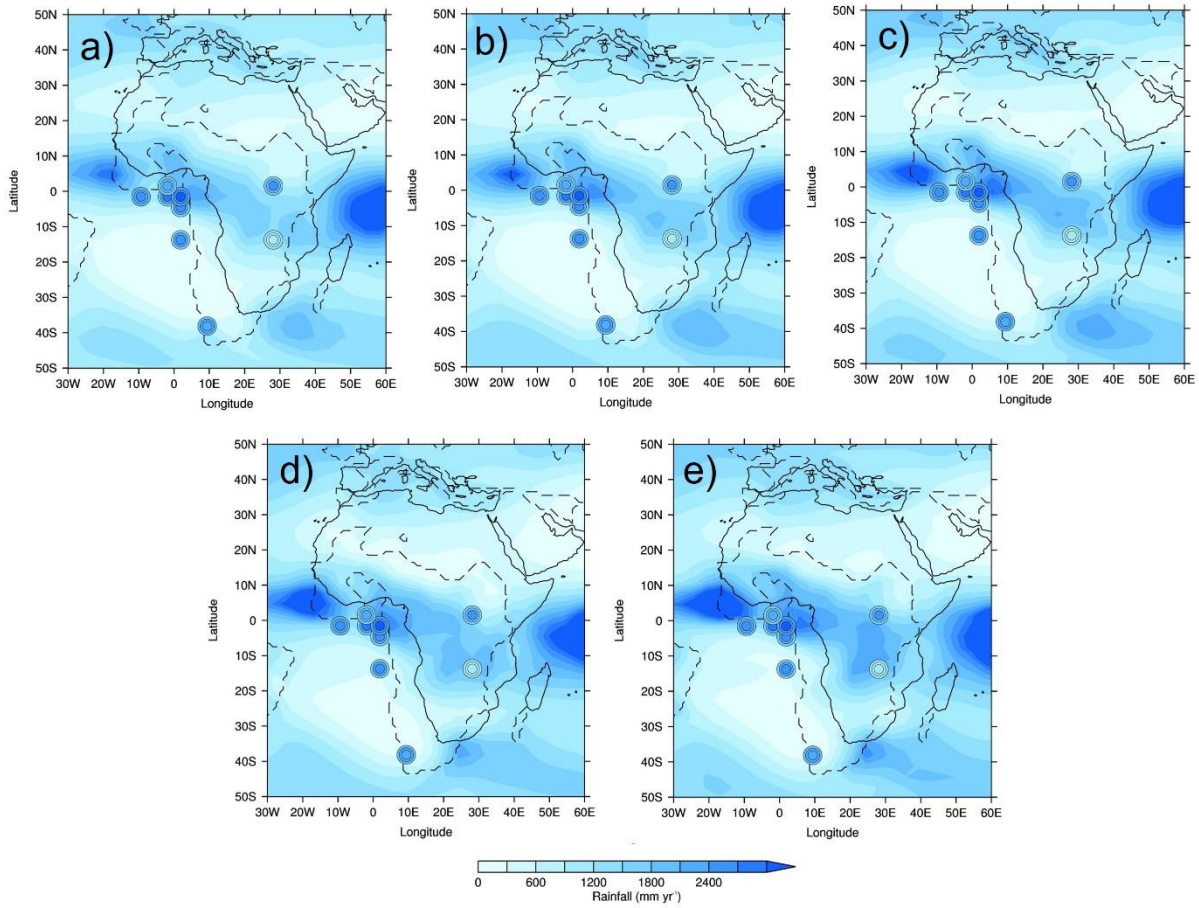

Figure 11 – Annual mean precipitation from reconstructions (circles) and CO_2 experiments multi-model ensemble mean (MME, background gridded data): a) 1x; b) 2x; c) 3x (lower-level CO_2 sample); d) 3x (higher level CO_2 sample); e) 6x. Concentric circles show 95% confidence interval for all sites except Mahenge, where they show +/- 1 standard deviation: outer circle = lower range (or -1 standard deviation), middle circle = average (or, for Mahenge, mode) and inner circle = upper range (or +1 standard deviation). Reconstructions have been rotated forwards to where they are in the PI. Solid lines show the PI mask and dashed lines show the Eocene mask. Note that, using the common spatial resolution of the MME, 3 reconstructions are all in the same location in West Africa (even though they are in different locations in reality); here, therefore, only the top-most reconstruction is shown

Quantitatively, the root mean squared error (RMSE) between each model (as well as the MME) and the reconstructions at every location is shown in Table 3 and, similar to the anomalies from each model as discussed above, there is no clear relationship between changing CO_2 and a better match to the reconstructions. Most models suggest a better fit to the reconstructions at lower levels of CO_2, such as CESM1.2_CAM5 where there is a general increase in RMSE as the CO_2 increases; however, this is not the case for every model, with for example GFDL_CM2.1 showing a better fit with reconstructions at 2x and 4x CO_2, rather than higher or lower levels (Table 3). For many of the models and the MME, the 3x CO_2 experiments are showing the least fit with reconstructions. The MME, from the lower-level (but not in the higher-level) CO_2 sample, agrees with this conclusion that

765 lower CO_2 is giving a slightly better match to the reconstructions, with RMSE values of 758 mm year^{-1}, 831 mm year^{-1}, 1385 mm year^{-1}, 889 mm year^{-1} and 839 mm year^{-1} for the 1x, 2x, 3x (lower-level CO_2 sample), 3x (higher-level CO_2 sample) and 6x experiments, respectively (Table 3).

768

	1x CO_2	**1.5x CO_2**	**2x CO_2**	**3x CO_2**	**4x CO_2**	**6x CO_2**	**9x CO_2**
CESM1.2_CAM5	681			750		704	822
COSMOS-landveg_r2413	699			1424	713		
GFDL_CM2.1	803		762	1027	786	975	
HadCM3B_M2.1aN	796		884	1988			
HadCM3BL_M2.1aN	816		1018	1742			
INM-CM4-8						966	
IPSLCM5A2		744		669			
MIROC4m	614		662	785			
NorESM1_F			1149		1522		
MME (lower-level CO_2 sample)	758		831	1385			
MME (higher-level CO_2 sample)				889		839	

769

770 Table 3 - Root Mean Squared Error (RMSE) for mean annual precipitation (MAP) between each model (and
771 multi-model ensemble mean, MME, using both samples) and reconstructions, for each CO_2 experiment

772

773 **4. DISCUSSION AND CONCLUSIONS**

774 This study has investigated African precipitation during the early Eocene, as simulated by the
775 DeepMIP models. This study is novel, because it investigates the relatively little-studied subject of
776 African hydroclimate during the early Eocene. The results of this study have been divided into four
777 separate sections, corresponding to the four questions posed in Section 1. Firstly, in Section 3.1 the
778 DeepMIP models' PI simulations have been compared to satellite-derived estimates of precipitation,
779 to ascertain how well the models are able to reproduce African precipitation under 'modern'
780 conditions (please see Section 2.3.1 for a discussion of the caveat that here the term 'modern' is
781 actually a combination of both pre-industrial and 20th-21st century). Secondly, in Section 3.2 the
782 DeepMIP models' Eocene simulations have been compared to both the PI simulations and each other,
783 to investigate the impact of non-CO_2 components (i.e. other boundary condition changes, such as to
784 the LSM) and CO_2 components (i.e. increasing CO_2) on African precipitation. Thirdly, in Section 3.3
785 the CO_2 driven response has been investigated further by looking at a number of dynamic and
786 thermodynamic fields simulated by the models, to ascertain possible physical mechanisms behind the
787 observed precipitation response. Lastly, in Section 3.4 the DeepMIP models' Eocene simulations
788 have been compared to newly-available proxy data, to indicate how well the models agree with
789 current best precipitation estimates from the Eocene.

The comparison between the DeepMIP PI simulations and modern observations (from TAMSAT) suggest that individual models are both underestimating or overestimating the spatial patterns of African precipitation; this is consistent with Monerie *et al*. (2020), who analysed a number of historical simulations from both CMIP5 and CMIP6 and found that the models' ability to reproduce observations was firstly model dependent and secondly geographically dependent, with many models underestimating precipitation over the Sahel and overestimating it over the Guinea coast and tropical Atlantic. However, here the MME is reducing these biases and is showing the best agreement with TAMSAT in terms of precipitation spatial patterns, highlighting the utility of the MME as a best estimate of the actual precipitation. This has been found elsewhere, such as by Ayugi *et al*. (2021) who looked at East African precipitation in both CMIP5 and CMIP6 models and again found a better performance of the MME relative to individual models, due to systematic errors in individual models being cancelled out. Moreover, Rougier *et al*. (2013) show that it is actually a statistical property of this type of analysis that the ensemble mean will always provide the best match to the data e.g. have the lowest RMSE. Concerning the latitudinal extent and seasonal timings of African precipitation, most models show a much wider (latitudinally) West African rain belt compared to TAMSAT and are not reproducing the rapid drop-off in precipitation near the Equator or north of 15°N. This is somewhat in contrast to Monerie *et al*. (2020), who noted that the majority of CMIP5 and CMIP6 models did not have the monsoon extending far enough to the north and were instead showing a southward displacement of precipitation maxima, relative to observations; however, that particular study used the models' historical simulations (as well as a different MME), not pre-industrial as shown here, which may explain the discrepancy. Outside of the JJA West African monsoon season most models are too wet, but within the monsoon season the results suggest that the drier models (i.e. those underestimating West African precipitation) are closer to modern observations than those that are too wet (i.e. overestimating West African precipitation).

The comparison between the DeepMIP Eocene simulations and the PI suggests that, when all individual models are considered separately, there is no obvious wetting or drying trend (relative to the PI) as the CO_2 increases. This is another reason to focus on the MME, which allows easier interpretation as the large model spread is removed. Concerning the non-CO_2 component of precipitation change (i.e. the impact of other boundary conditions when CO_2 is kept at PI levels), the results suggest that changes to the LSM may be responsible for the increases in precipitation (relative to the PI) to the north of Eocene Africa and the western Indian Ocean, given that these are 'newly exposed' regions of ocean in the Eocene, thereby providing a larger moisture source. In contrast, it is likely that changes in vegetation are responsible for the region of drying (relative to the PI) over equatorial Eocene Africa, because regions of tropical rainforest during the PI were instead savanna and desert during the Eocene, thereby reducing the amount of evapotranspiration and evaporation. It

should be noted, though, that validation of the Eocene vegetation over certain regions of Africa was not possible when creating this boundary condition (Herold *et al*. 2014), therefore there is a level of uncertainty here. When the Eocene precipitation is rotated forwards in time to where it is in the PI, a similar pattern is shown but is more pronounced, and suggests a northward displacement of the primary rain belt (relative to today), which is consistent with previous work (e.g. Carmichael *et al*. 2016). However, this is in contrast to when CO_2 is increased in the Eocene simulations. Concerning this CO_2 component of precipitation change, at the lower levels of increased CO_2 (such as 2x and 3x that of the PI) precipitation over the equatorial Atlantic and West Africa appears to be increasing in response to rising CO_2, with the concomitant decrease in precipitation north of the equator suggesting a possible displacement of the Atlantic ITCZ towards the south. This therefore suggests that the boundary condition changes imposed for the Eocene are resulting in a northward displacement of the primary rain belt, but increasing CO_2 (with the same boundary conditions) is resulting in a southward displacement of the primary rain belt. At even higher levels of CO_2 (such as 6x that of the PI), precipitation over West Africa is more enhanced relative to the lower levels, but the region of drying is less evident. The enhancement of Northern Hemisphere summer West African precipitation at the highest levels of CO_2 is again consistent with previous work, such as that of Carmichael *et al*. (2016) who showed a generally more intense hydrological cycle at higher CO_2 levels and that of Carmichael *et al*. (2018) who demonstrated an increase in precipitation extremes over tropical Africa at higher CO_2 levels.

Consistent with Carmichael *et al*. (2016), the precipitation increases over West Africa as CO_2 concentrations rise are associated with increased SAT, a strongly positive the P-E balance and cloud cover increases and, concerning temperature, as such are consistent with the idea that a generally warmer world results in a generally wetter world; the 'wet-gets-wetter and dry-gets-drier' hypothesis (e.g. Held and Soden 2006). However, the largest increases in SAT shown here are over southern Africa, not where the largest precipitation increases are seen, suggesting factors other than a generally warming world (i.e. dynamical changes) are responsible for the localised precipitation response. Both the region of enhanced precipitation over West Africa, and the region of drying in the equatorial Atlantic around 10°N, may be explained by low-level circulation changes. Up to 3x that of the PI CO_2, clockwise low-level circulation increases with CO_2, drawing in more moisture from the equatorial Atlantic and causing a relative drying further north, hence the appearance of a southward displacement of the Atlantic ITCZ. At higher levels of CO_2, however, where increases in West African precipitation are shown but the region of drying around 10°N is not, the increased clockwise low-level circulation is replaced by increased south-westerly flow; here, therefore, precipitation is being enhanced by more moisture being drawn in by this south-westerly flow from the warm South Atlantic.

Lastly, the results from the model-data comparison suggests that whether the Eocene simulations (regardless of CO_2 experiment) over- or underestimate African precipitation is highly geographically dependent, with some of the CO_2 experiments at some of the locations lying within the uncertainty range of the reconstructions but others being too wet or too dry. There is some suggestion of a latitudinal relationship, with the simulations overestimating precipitation near the Equator and underestimating precipitation in high latitude regions, such as South Africa; this latter point is consistent with the findings of Carmichael *et al*. (2016). Whether the models are considered independently or whether the MME is used, the results suggest a marginally better fit with the reconstructions at lower levels of CO_2, and this is in contrast (indirectly) to the findings of Carmichael *et al*. (2016) who suggested the warmest models in the regions of increased precipitation best matched the data; it should be noted, however, that this was a global study. There is no evidence for this here, and indeed the finding of a better match at lower levels of CO_2 is in contrast to that of Reichgelt *et al*. (2021, in prep) who focused on Australia and found that the higher, 6x CO_2 experiment was the best match to reconstructions. However, given the uncertainties associated with both the reconstructions (discussed above) and the boundary conditions used to force the models, it is difficult to draw firm conclusions from a model-data comparison of this type. Moreover, a particularly big problem here is that, despite the newly-compiled reconstructions presented here, there is still a lack of data across Africa, hindering any firm conclusions.

In conclusion, therefore, this study has shown that the DeepMIP models are able to approximately reproduce the modern African precipitation and, in response to rising CO_2, suggest an enhancement of precipitation in this region associated with increasing temperatures and changes to low-level circulation. At very high levels of CO_2 the models may be too wet, relative to reconstructions. However, this might be because the NLR proxy approach has difficulty generating MAP values above modern, or connected to the relatively few data points within the reconstructions. Using the MME provides the clearest suggestion of this, but the large amount of model spread means that when individual models are considered, either relative to their corresponding PI simulations or reconstructions, no clear relationship is shown.

DATA AVAILABILITY

TAMSAT data are publicly available to download at https://www.tamsat.org.uk/. The palaeobotanical precipitation estimates compiled here are available as a spreadsheet included in the Supplementary Material. The DeepMIP PI and Eocene simulations are available by following the instructions at https://www.deepmip.org/data-eocene/.

AUTHOR CONTRIBUTIONS

CJRW carried out the analysis, produced the figures, wrote the manuscript and led the paper; all authors contributed to writing subsequent drafts of the paper. DJL also carried out some of the analysis, and provided guidance on the scientific discussion. WLC, AAO, YD, DKH, AMB, JBL, PAM, IN, GK, SS, ZZ and JZ carried out the underlying DeepMIP model simulations. US, DRG, GNI and TR collated and synthesised the proxy data. MH and BLOB provided guidance on the scientific discussion and analysis.

COMPETING INTERESTS

The authors declare that they have no conflict of interest.

ACKNOWLEDGEMENTS

CJRW acknowledges the financial support of the UK Natural Environment Research Council funded SWEET project (Super-Warm Early Eocene Temperatures), and that of the European Research Council. WLC and AAO acknowledge funding from JSPS KAKENHI and MEXT KAKENHI, and are grateful to JAMSTEC for use of the Earth Simulator. The numerical simulations performed by DKH and AMB used resources provided by the Swedish National Infrastructure for Computing (SNIC) at the National Supercomputer Centre (NSC), partially funded by the Swedish Research Council. YD and JBL thank GENCI for providing access to the HPC resources of TGCC. PAM thanks Evgeny Volodin and INM RAS for the help with INMCM simulations. GK acknowledges financial support by PACES through the Helmholtz association and the computing centre of the Alfred Wegener Institute in Bremerhaven and the DKRZ in Hamburg (Germany) for computational resources, infrastructure and support. JZ and BLOB acknowledge support from the National Center for Atmospheric Research, which is a major facility sponsored by the National Science Foundation. US acknowledges funding from the Natural Environment Research Council. DRG acknowledges funding from the Natural Sciences and Engineering Council of Canada. GNI acknowledges a GCRF Royal Society Dorothy Hodgkin Fellowship.

FINANCIAL SUPPORT

CJRW was supported by the UK Natural Environment Research Council-funded SWEET project (grant no. NE/P01903X/1) and that of the European Research Council under the European Union's Seventh Framework Programme (FP/2007-868 2013) (ERC grant agreement no. 340923 (TGRES)). WLC and AAO were supported by JSPS KAKENHI (grant no. 17H06104) and MEXT KAKENHI (grant no. 17H06323). DKH and AMB were partially funded by the Swedish Research Council through grant agreement no. 2018-05973 and 2016-03912, and DKH also acknowledges the support of FORMAS grant 2018-01621 and Australian Research Council grant DE220100279. YD and JBL were supported by GENCI under allocation no. 2019-A0050102212. PAM was supported by the state

assignment project no. AAAA-A19-119022190173-2 (FMGE-2019-0009). JZ and BLOB were supported by the National Science Foundation under cooperative agreement no. 1852977. US was supported by the Natural Environment Research Council (grant NE/P019137/1). DRG was supported by the Natural Sciences and Engineering Council of Canada (grant no. 2016-04337). GNI was supported by a GCRF Royal Society Dorothy Hodgkin Fellowship (DHF\R1\191178).

945 **LIST OF TABLES**

956

957 **LIST OF FIGURES**

precipitation rotated forward to where it is in the PI. Note that in a), solid lines show the PI mask and dashed lines show the Eocene mask

Figure 6 – JJA precipitation multi-model ensemble mean (MME) climatology absolutes and anomalies for the 1x, 2x, 3x and 6x CO_2 experiments, using both samples: a) Lower-level sample of CO_2 experiments (comprising the four models that conducted these: GFDL_CM2.1, HadCM3B_M2.1aN, HadCM3BL_M2.1aN and MIROC4m), absolutes (top row) and anomalies (second row); b) Higher-level sample of CO_2 experiments (comprising the two models that conducted these: CESM1.2_CAM5 and GFDL_CM2.1), absolutes (top row) and anomalies (second row)

Figure 7 – Same as Figure 6 but for JJA 1.5 m surface air temperature

Figure 8 – JJA P-E multi-model ensemble mean (MME) climatology absolutes for the 1x, 2x, 3x and 6x CO_2 experiments, using both samples: a) Lower-level sample of CO_2 experiments (comprising the four models that conducted these: GFDL_CM2.1, HadCM3B_M2.1aN, HadCM3BL_M2.1aN and MIROC4m), PI (top row) and Eocene (bottom row); b) Higher-level sample of CO_2 experiments (comprising the two models that conducted these: CESM1.2_CAM5 and GFDL_CM2.1), PI (top row) and Eocene (bottom row). Note that the PI panels are identical in each sample because they contain the same models, but are simply replicated here for ease of comparison

Figure 9 – Same as Figure 6 but for JJA 850 mb wind

Figure 10 – Annual mean precipitation from reconstructions (black) and CO_2 experiments multi-model ensemble mean (MME, colours) at each individual location. Uncertainty in reconstructions is measured by 95% confidence interval for all sites except Mahenge, where they show +/- 1 standard deviation. Locations have been ordered according to the reconstructions' values, lowest to highest. Note that locations 1-4 and 6-8 are all in the same location, but from different stages during the Lutetian (~41-47 Ma), and so have been re-sampled and averaged into one overall mean (location 5)

Figure 11 – Annual mean precipitation from reconstructions (circles) and CO_2 experiments multi-model ensemble mean (MME, background gridded data): a) 1x; b) 2x; c) 3x (lower-level CO_2 sample); d) 3x (higher level CO_2 sample); e) 6x. Concentric circles show 95% confidence interval for all sites except Mahenge, where they show +/- 1 standard deviation: outer circle = lower range (or -1 standard deviation), middle circle = average (or, for Mahenge, mode) and inner circle = upper range (or +1 standard deviation). Reconstructions have been rotated forwards to where they are in the PI. Solid lines show the PI mask and dashed lines show the Eocene mask. Note that, using the common spatial resolution of the MME, 3 reconstructions are all in the same location in West Africa (even

though they are in different locations in reality); here, therefore, only the top-most reconstruction is shown

LIST OF SUPPLEMENTARY TABLES/FIGURES

Table S1 - Paleocene-Eocene palaeobotanical records from Africa. Note that the eight sites at Mahenge are from slightly different time-slices within the Lutetian, and have therefore been averaged when making the model-data comparison. Moreover, these sites were generated by Leaf Area Analysis (LAA), not Nearest Living Relative (NLR) estimates, therefore do not have associated taxa. Note also that the exact ages of each site, and which best overlap with the DeepMIP simulations, is uncertain; the simulations represent ~50 Ma, whereas the Ypresian sites span ~47-56 Ma, the Lutetian sites span ~41-47 Ma and the Paleocene sites are generally ~56 Ma and earlier.

Table S2 - Geodetic coordinates of occurrences from the Global Biodiversity Information Facility (GBIF)

Figure S1 – Topography/bathymetry changes in DeepMIP simulations. Solid line shows PI land sea mask, dashed line shows Eocene land sea mask

Figure S2 – JJA sea surface temperature (SST) climatologies from each model conducting the 1x CO_2 experiment, as well as multi-model ensemble mean (MME): a) PI; b) Eocene

Figure S3 - JJA climatologies for each CO_2 simulation from each model: a) 1.5 m surface air temperature (SAT); b) JJA Precipitation - Evaporation (P-E); c) 850 mb vector winds. Note that in b), evaporation data are missing from NorESM1_F, hence its exclusion here, and likewise in c), wind data are missing from INM-CM4-and IPSLCM5A2, hence their exclusion here

Figure S4 – Approximate locations of reconstructions across Africa, ordered according to the reconstructions' values, lowest to highest. Note that locations 1-9 are all in the same location, but from different stages during the Lutetian (~41-47 Ma), and so have been re-sampled and averaged into one overall mean (location 5). Reconstructions have been rotated forwards to where they are in the PI. Solid lines show the PI mask and dashed lines show the Eocene mask.

Figure S5 - Annual mean precipitation from reconstructions (circles) and CO_2 experiments (background gridded data) for each individual model. Locations in Mahenge, Tanzania are in the same place, so have been averaged. Reconstructions have been rotated forwards to where they are in the PI. Note that, for the majority of models, the spatial resolution is such that 3 reconstructions are

all in the same location in West Africa (even though they are in different locations in reality); here, therefore, only the top-most reconstruction is shown

REFERENCES

Adeonipekun, P. A., Ehinola, O. A., Yussuph, I. A., Toluhi, A. and Oyelami, A.: Bio-sequence stratigraphy of Shagamu Quarry outcrop, Benin Basin, southwestern Nigeria, World Applied Sciences Journal, 18, 91-106, DOI: 10.5829/idosi.wasj.2012.18.01.3572, 2012.

Anagnostou, E., John, E. H., Babila, T. L., Sexton, P. F., Ridgwell, A., Lunt, D. J., Pearson, P. N., Chalk, T. B., Pancost, R. D. and Foster, G. L.: Proxy evidence for state-dependence of climate sensitivity in the Eocene greenhouse, Nature Communications, 11(4436), https://doi.org/10.1038/s41467-020-17887-x, 2020.

Anagnostou, E., John, E. H., Edgar, K. M., Foster, G. L., Ridgwell, A., Inglis, G. N., Pancost, R. D., Lunt D. J. and Pearson, P. N.: Changing atmospheric CO2 concentration was the primary driver of early Cenozoic climate, Nature, 533, 380–384, https://doi.org/10.1038/nature17423, 2016.

Arakawa, A. and Schubert, W. H.: Interactions of cumulus cloud ensemble with the large-scale environment. Part I, J. Atmos. Sci., 31, 671-701, https://doi.org/10.1175/1520-0469(1974)031<0674:IOACCE>2.0.CO;2, 1974.

Arias, P. A., Bellouin, N., Coppola, E. et al.: Technical Summary. In Climate Change 2021: The Physical Science Basis. Contribution of Working Group I to the Sixth Assessment Report of the Intergovernmental Panel on Climate Change [Masson-Delmotte, V., Zhai, P., Pirani, A., Connors, S. L., Péan, C., Berger, S., Caud, N., Chen, Y., Goldfarb, L., Gomis, M. I., Huang, M., Leitzell, K., Lonnoy, E., Matthews, J. B. R., Maycock, T. K., Waterfield, T., Yelekçi, O., Yu, R. and Zhou, B. (eds.)], Cambridge University Press, In Press, https://www.ipcc.ch/report/ar6/wg1/#TS, 2021.

Atta-Peters, D. and Salami, M. B.: Late Cretaceous to early Tertiary pollen grains from offshore Tano Basin, southwestern Ghana, Revista Española de Micropaleontologia, 36(3), 451-465, https://dialnet.unirioja.es/servlet/articulo?codigo=1070295, 2004.

Ayugi, B., Zhihong, J., Zhu, H., Ngoma, H., Babaousmail, H., Rizwan, K. and Dike, V.: Comparison of CMIP6 and CMIP5 models in simulating mean and extreme precipitation over East Africa, Int. J. Clim., https://doi.org/10.1002/joc.7207, 2021.

Beerling, D. J., Fox, A. and Anderson, C. W.: Quantitative uncertainty analyses of ancient atmospheric CO_2 estimates from fossil leaves, AJS, 309(9), 775-787, DOI: https://doi.org/10.2475/09.2009.01, 2009.

Betts, K.: A new convective adjustment scheme. Part 1. Observational and theoretical basis, Q. J. R.Meteorol. Soc. 112, 677-691, https://doi.org/10.1002/qj.49711247307, 1986.

Bijl, P. K., Houben, A. J. P., Schouten, S., Bohaty, S. M., Sluijs, A., Reichart, G.-J., Sinninghe Damsté J. S. and Brinkhuis, H.: Transient middle Eocene atmospheric CO_2 and temperature variations, Science, 330(6005), 819-821, DOI: 10.1126/science.1193654, 2010.

Bony, S. and Emanuel, K. A.: A parameterization of the cloudiness associated with cumulus convection; evaluation using TOGA COARE data, J. Atmos. Sci., 58(21), 3158-3183, https://doi.org/10.1175/1520-0469(2001)058<3158:APOTCA>2.0.CO;2, 2001.

Braconnot, P., Harrison, S. P., Otto-Bliesner, B. L., Abe-Ouchi, A., Jungclaus, J. and Peterchmitt, J.-Y.: The palaeoclimate modelling intercomparison project contribution to CMIP5, CLIVAR Exch. Newsl, 56, 15–19, 2011.

Braconnot, P., Otto-Bliesner, B., Harrison, S., Joussaume, S., Peterchmitt, J.-Y., Abe-Ouchi, A., Crucifix, M., Driesschaert, E., Fichefet, Th., Hewitt, C. D., Kageyama, M., Kitoh, A., Laîné, A., Loutre, M.-F., Marti, O., Merkel, U., Ramstein, G., Valdes, P., Weber, S. L., Yu, Y., and Zhao, Y.: Results of PMIP2 coupled simulations of the Mid-Holocene and Last Glacial Maximum – Part 1: experiments and large-scale features, Clim. Past, 3, 261-277, https://doi.org/10.5194/cp-3-261-2007, 2007.

Bushell, A. C.: Chapter 2 Understanding the Unified Model (Section 2.1.1), in Matthews, D.: Unified Model User Guide, http://www.ukscience.org/_Media/UM_User_Guide.pdf, Accessed 22/9/21, 1998.

Cantrill, D. J., Bamford, M. K., Wagstaff, B. E. and Sauquet, H.: Early Eocene fossil plants from the Mwadui kimberlite pipe, Tanzania, Review of Palaeobotany and Palynology, 196, 19-35, DOI: 10.1016/j.revpalbo.2013.04.002, 2013.

Carmichael, M. J., Lunt, D. J., Huber, M., Heinemann, M., Kiehl, J., LeGrande, A., Loptson, C. A., Roberts, C. D., Sagoo, N., Shields, C., Valdes, P. J., Winguth, A., Winguth, C. and Pancost, R. D.: A model-model and data-data comparison for the early Eocene hydrological cycle, Clim. Past, 12, 455-481, doi:10.5194/cp-12-455-2016, 2016.

Carmichael, M. J., Pancost, R. D. and Lunt D. J.: Changes in the occurrence of extreme precipitation events at the Paleocene–Eocene thermal maximum, Earth Planet. Sci. Lett., 501, 24-36, https://doi.org/10.1016/j.epsl.2018.08.005, 2018.

Chan, W.-L., Abe-Ouchi, A. and Ohgaito, R.: Simulating the mid- Pliocene climate with the MIROC general circulation model: experimental design and initial results, Geosci. Model Dev., 4, 1035-1049, https://doi.org/10.5194/gmd-4-1035-2011, 2011.

Chiaghanam, O. I., Chiadikobi, K.C., Oguanya, C.E., Ikegwuonu, O.N., Nwokeabia, C.N.: Palynological and Paleoenvironmental Study of Paleogene in Bende - Umuahia, Niger Delta Basin, Nigeria, Journal of Environment and Earth Science, 7, 97-107, ISSN 2225-0948, 2017.

Cox, P. M.: A primitive equation, 3-dimensional model of the ocean, GFDL Ocean Group Technical Report No. 1, Geophysical Fluid Dynamics Laboratory, Princeton, New Jersey, 1984.

Cox, P. M., Betts, R. A., Bunton, C. B., Essery, R. L. H., Rowntree, P. R. & Smith, J.: The impact of new land surface physics on the GCM simulation of climate and climate sensitivity. Clim. Dyn., 15(3), 183-203. https://doi.org/10.1007/s003820050276, 1999.

de Villiers, S. E.: The palynology of Tertiary sediments from a palaeochannel in Namaqualand, Doctor of Philosophy thesis, Faculty of Science, University of Witwatersrand, Johannesburg, 100 pp., 1997.

Delworth, T. L., Broccoli, A. J., Rosati, A., Stouffer, R. J., Balaji, V., Beesley, J. A., Cooke,W. F., Dixon, K.W., Dunne, J., Dunne, K. A., Durachta, J. W., Findell, K. L., Ginoux, P., Gnanadesikan, A., Gordon, C. T., Griffies, S. M., Gudgel, R., Harrison, M. J., Held, I. M., Hemler, R. S., Horowitz, L. W., Klein, S. A., Knutson, T. R., Kushner, P. J., Langenhorst, A. R., Lee, H.-C., Lin, S.-J., Lu, J., Malyshev, S. L., Milly, P. C. D., Ramaswamy, V., Russell, J., Schwarzkopf, M. D., Shevliakova, E., Sirutis, J. J., Spelman, M. J., Stern, W. F., Winton, M., Wittenberg, A. T., Wyman, B., Zeng, F. and Zhang, R.: GFDL's CM2 Global Coupled Climate Models. Part I: Formulation and Simulation Characteristics, J. Climate, 19, 643–674, https://doi.org/10.1175/JCLI3629.1, 2006.

Dufresne, J.-L., Foujols, M.-A., Denvil, S., Caubel, A., Marti, O., Aumont, O., Balkanski, Y., Bekki, S., Bellenger, H., Benshila, R., Bony, S., Bopp, L., Braconnot, P., Brockmann, P., Cadule, P., Cheruy, F., Codron, F., Cozic, A., Cugnet, D., de Noblet, N., Duvel, J.-P., Ethé, C., Fairhead, L., Fichefet, T., Flavoni, S., Friedlingstein, P., Grandpeix, J.-Y., Guez, L., Guilyardi, E., Hau all glustaine, D., Hourdin, F., Idelkadi, A., Ghattas, J., Joussaume, S., Kageyama, M., Krinner, G., Labetoulle, S., Lahellec, A., Lefebvre, M.-P., Lefevre, F., Levy, C., Li, Z. X., Lloyd, J., Lott, F., Madec, G., Mancip, M., Marchand, M., Masson, S., Meurdesoif, Y., Mignot, J., Musat, I., Parouty, S., Polcher, J., Rio, C., Schulz, M., Swingedouw, D., Szopa, S., Talandier, C., Terray, P., Viovy, N. and Vuichard, N.:

Climate Change Projections Using the IPSL-CM5 Earth System Model: From CMIP3 to CMIP5, Clim. Dynam., 40, 2123-2165, https://doi.org/10.1007/s00382-012-1636-1, 2013.

Durre I., Menne, M. J., Gleason, B. E., Houston, T. G. and Vose, R. S.: Comprehensive automated quality assurance of daily surface observations, J. Applied Meteor. and Climatol., 49, 1615-1633, doi.10.1175/2010JAMC2375.1, 2010.

Durre I., Menne, M. J. and Vose, R. S.: Strategies for evaluating quality assurance procedures, J. Applied Meteor. and Climatol., 47, 1785-1791, doi:10.1175/2007JAMC1706.1, 2008.

Eaton, B.: User's Guide to the Community Atmosphere Model CAM-CAM-5.1.1, NCAR (https://www.cesm.ucar.edu/models/cesm1.0/cam/docs/ug5_1_1/ug.html), Accessed 10/9/21, 2010.

Edwards, J. M. and Slingo, A.: Studies with a flexible new radiation code. I: Choosing a configuration for a large-scale model. Q.J.R. Meteorol. Soc., 122: 689-719. https://doi.org/10.1002/qj.49712253107, 1996.

Eisawi, A. and Schrank, E.: Upper Cretaceous to Neogene palynology of the Melut Basin, southeast Sudan, Palynology, 32, 101-129, DOI: 10.1080/01916122.2008.9989653, 2008.

Emanuel, K. A.: A scheme for representing cumulus convection in large-scale models, J. Atmos. Sci., 48(21), 2313-2329, https://doi.org/10.1175/1520-0469(1991)0482.0.CO;2, 1991.

Eyring, V., Bony, S., Meehl, G. A., Senior, C. A., Stevens, B., Stouffer, R. J., and Taylor, K. E.: Overview of the Coupled Model Intercomparison Project Phase 6 (CMIP6) experimental design and organization, Geosci. Model Dev., 9, 1937-1958, doi:10.5194/gmd-9-1937-2016, 2016.

Farnsworth, A., Lunt, D. J., Robinson, S.A., Valdes, P.J., Roberts, W.H.G., Clift, P.D., Markwick, P., Su, T., Wrobel, N., Bragg, F., Kelland, S.J. and Pancost, R.D.: Past East Asian monsoon evolution controlled by paleogeography, not CO2. Science Advances, 5, 10, DOI: 10.1126/sciadv.aax1697, 2019.

Fouquart, Y. and Bonnel, B.: Computations of solar heating of the Earth's atmosphere: A new parameterization, Beitr. Phys. Atmos., 53, 35-62, 1980.

Funk, C., Nicholson, S., Landsfeld, M., Klotter, D., Peterson, P. and Harrison, L.: The Centennial Trends Greater Horn of Africa precipitation dataset, Sci Data 2, 150050, https://doi.org/10.1038/sdata.2015.50, 2015.

Galbraith, E. D., Kwon, E. Y., Gnanadesikan, A., Rodgers, K. B., Griffies, S. M., Bianchi, D., Sarmiento, J. L., Dunne, J. P., Simeon, J., Slater, R. D., Wittenberg, A. T. and Held, I. M.: Climate Variability and Radiocarbon in the CM2Mc Earth System Model, J. Clim., 24, 4230-4254, https://doi.org/10.1175/2011JCLI3919.1, 2011.

Goha, R. B., Zeli, B. D., Konan, R. Y., Tea-Yassi, J., Kouadio, D. K. and Tahi, I.: Stratigraphie palynologique du Maastrichtien supérieur-Eocène supérieur du bassin sédimentaire offshore de Côte d'Ivoire, Afrique de l'ouest, International Journal of African Studies, 6, 40-57, 2016.

Grant, A.: Chapter 2 Understanding the Unified Model (Section 2.1.6), in Matthews, D.: Unified Model User Guide, http://www.ukscience.org/_Media/UM_User_Guide.pdf, Accessed 22/9/21, 1998.

Guo, C., Bentsen, M., Bethke, I., Ilicak, M., Tjiputra, J., Toniazzo, T., Schwinger, J. and Otterå, O. H.: Description and evaluation of NorESM1_F: a fast version of the Norwegian Earth System Model (NorESM), Geosci. Model Dev., 12, 343-362, https://doi.org/10.5194/gmd-12-343-2019, 2019.

Hack, J. J.: Parameterization of moist covection in the NCAR Community Climate Model CCM2, J. Geophys. Res. Atmos., 99(D3): 5551-5568, DOI:10.1029/93JD03478, 1994.

Hagemann, S.: An improved land surface parameter dataset for global and regional climate models, Max Planck Institute for Meteorology, Report No. 336, https://citeseerx.ist.psu.edu/viewdoc/download?doi=10.1.1.471.2882&rep=rep1&type=pdf, Accessed 17/9/21, 2002.

Harrison, S. P. and Prentice, I. C.: Climate and CO_2 controls on global vegetation distribution at the last glacial maximum: analysis based on palaeovegetation data, biome modelling and palaeoclimate simulations, Glob. Change Bio., 9 (7), 983-1004, https://doi.org/10.1046/j.1365-2486.2003.00640.x, 2003.

Harrison, S. P., Bartlein, P. J., Brewer, S., Prentice, I. C., Boyd, M., Hessler, I., Holmgren, K., Izumi, K. and Willis, K.: Climate model benchmarking with glacial and mid-Holocene climates, Clim. Dyn., 43, 671-688, https://doi.org/10.1007/s00382-013-1922-6, 2014.

Hasumi, H.: CCSR Ocean Component Model (COCO) Version 2.1, Technical Report, The University of Tokyo, Tokyo, Japan, 2000.

Haywood, A. M., Tindall, J. C., Dowsett, H. J., Dolan, A. M., Foley, K. M., Hunter, S. J., Hill, D. J., Chan, W.-L., Abe-Ouchi, A., Stepanek, C., Lohmann, G., Chandan, D., Peltier, W. R., Tan, N., Contoux, C., Ramstein, G., Li, X., Zhang, Z., Guo, C., Nisancioglu, K. H., Zhang, Q., Li, Q., Kamae, Y., Chandler, M. A., Sohl, L. E., Otto-Bliesner, B. L., Feng, R., Brady, E. C., von der Heydt, A. S., Baatsen, M. L. J. and Lunt, D. J.: The Pliocene Model Intercomparison Project Phase 2: large-scale climate features and climate sensitivity, Clim. Past, 16, 2095-2123, https://doi.org/10.5194/cp-16-2095-2020, 2020.

Held, I. M. and Soden, B. J.: Robust Responses of the Hydrological Cycle to Global Warming, J. Clim., 19 (21), 5686-5699, DOI: https://doi.org/10.1175/JCLI3990.1, 2006.

Herold, N., Buzan, J., Seton, M., Goldner, A., Green, J. A. M., Müller, R. D., Markwick, P. and Huber, M.: A suite of early Eocene (~55 Ma) climate model boundary conditions, Geosci. Model Dev., 7, 2077-2090, doi:10.5194/gmd-7-2077-2014, 2014.

Hijmans, R. J., Cameron, S. E., Parra, J. L., Jones, P. G. and Jarvis, A.: Very high resolution interpolated climate surfaces for global land areas, Int. J. Clim., 25, 1965-1978, https://doi.org/10.1002/joc.1278, 2005.

Huber, M. and Caballero, R.: The early Eocene equable climate problem revisited, Clim. Past, 7, 603-633, doi:10.5194/cp-7-603-2011, 2011.

Hurrell, J. W., Holland, M. M., Gent, P. R., Ghan, S., Kay, J. E., Kushner, P. J., Lamarque, J. F., Large, W. G., Lawrence, D., Lindsay, K., Lipscomb, W. H., Long, M. C., Mahowald, N., Marsh, D. R., Neale, R. B., Rasch, P., Vavrus, S., Vertenstein, M., Bader, D., Collins, W. D., Hack, J. J., Kiehl, J. T. and Marshall, S.: The community earth system model: A framework for collaborative research, B. Am. Meteorol. Soc., 94, 1339-1360, https://doi.org/10.1175/BAMS-D-12-00121.1, 2013.

Hutchinson, D. K., de Boer, A. M., Coxall, H. K., Caballero, R., Nilsson, J. and Baatsen, M.: Climate sensitivity and meridional overturning circulation in the late Eocene using GFDL CM2.1, Clim. Past, 14, 789-810, https://doi.org/10.5194/cp-14-789-2018, 2018.

Hollis, C. J., Dunkley Jones, T., Anagnostou, E., Bijl, P. K., Cramwinckel, M. J., Cui, Y., Dickens, G. R., Edgar, K. M., Eley, Y., Evans, D., Foster, G. L., Frieling, J., Inglis, G. N., Kennedy, E. M.,

Kozdon, R., Lauretano, V., Lear, C. H., Littler, K., Lourens, L., Meckler, A. N., Naafs, B. D. A., Pälike, H., Pancost, R. D., Pearson, P. N., Röhl, U., Royer, D. L., Salzmann, U., Schubert, B. A., Seebeck, H., Sluijs, A., Speijer, R. P., Stassen, P., Tierney, J., Tripati, A., Wade, B., Westerhold, T., Witkowski, C., Zachos, J. C., Zhang, Y. G., Huber, H. and Lunt, D. J.: The DeepMIP contribution to PMIP4: methodologies for selection, compilation and analysis of latest Paleocene and early Eocene climate proxy data, incorporating version 0.1 of the DeepMIP database, Geosci. Model Dev., 12, 3149–3206, https://doi.org/10.5194/gmd-12-3149-2019, 2019.

Holtslag, A. and Boville, B.: Local versus nonlocal boundary-layer diffusion in a global climate model, J. Clim., 6, 1825-1825, https://doi.org/10.1175/1520-0442(1993)006<1825:LVNBLD>2.0.CO;2, 1993.

Hyland, E., Sheldon, N. D. and Fan, M.: Terrestrial paleoenvironmental reconstructions indicate transient peak warming during the early Eocene climatic optimum, Geol. Soc. Am. Bull., 125(7-8), 1338-1348, DOI:10.1130/B30761.1, 2013.

Inglis, G. N., Bragg, F., Burls, N. J., Cramwinckel, M. J., Evans, D., Foster, G. L., Huber, M., Lunt, D. J., Siler, N., Steinig, S., Tierney, J. E., Wilkinson, R., Anagnostou, E., de Boer, A. M., Dunkley Jones, T., Edgar, K. M., Hollis, C. J., Hutchinson, D. K., and Pancost, R. D.: Global mean surface temperature and climate sensitivity of the early Eocene Climatic Optimum (EECO), Paleocene–Eocene Thermal Maximum (PETM), and latest Paleocene, Clim. Past, 16, 1953-1968, https://doi.org/10.5194/cp-16-1953-2020, 2020.

IPCC: Climate Change 2013: The Physical Science Basis. Contribution of Working Group I to the Fifth Assessment Report of the Intergovernmental Panel on Climate Change [Stocker, T. F., D. Qin, G.-K. Plattner, M. Tignor, S. K. Allen, J. Boschung, A. Nauels, Y. Xia, V. Bex and P. M. Midgley (eds.)], Cambridge University Press, Cambridge, United Kingdom and New York, NY, USA, pp 1535, https://www.ipcc.ch/report/ar5/wg1/, 2013.

IPCC: Climate Change 2021: The Physical Science Basis. Contribution of Working Group I to the Sixth Assessment Report of the Intergovernmental Panel on Climate Change [Masson-Delmotte, V., P. Zhai, A. Pirani, S.L. et al. (eds.)], Cambridge University Press, Cambridge, United Kingdom, https://www.ipcc.ch/report/ar6/wg1/, 2021.

Jacobs, B. F. and Herendeen, P. S.: Eocene dry climate and woodland vegetation in tropical Africa reconstructed from fossil leaves from northern Tanzania, Palaeogeography, Palaeoclimatology, Palaeoecology, 213, 115-123, 10.1016/S0031-0182(04)00368-2, 2004.

Jungclaus, J. H., Keenlyside, N., Botzet, M., Haak, H., Luo, J.-J., Latif, M., Marotzke, J., Mikolajewicz, U. and Roeckner, E.: Ocean circulation and tropical variability in the coupled model ECHAM5/MPI-OM, J. Climate, 19, 3952-3972, https://doi.org/10.1175/JCLI3827.1, 2006.

K-1 model developers: K-1 coupled model (MIROC) description, Technical Report, Center for Climate System Research (University of Tokyo), National Institute for Environmental Studies, Frontier Research Center for Global Change, Tokyo, Japan, 2004.

Kageyama, M., Braconnot, P., Harrison, S. P., Haywood, A. M., Jungclaus, J. H., Otto-Bliesner, B. L., Peterschmitt, J.-Y., Abe-Ouchi, A., Albani, S., Bartlein, P. J., Brierley, C., Crucifix, M., Dolan, A., Fernandez-Donado, L., Fischer, H., Hopcroft, P. O., Ivanovic, R. F., Lambert, F., Lunt, D. J., Mahowald, N. M., Peltier, W. R., Phipps, S. J., Roche, D. M., Schmidt, G. A., Tarasov, L., Valdes, P. J., Zhang, Q. and Zhou, T.: The PMIP4 contribution to CMIP6 – Part 1: Overview and over-arching analysis plan, Geosci. Model Dev., 11, 1033–1057, https://doi.org/10.5194/gmd-11-1033-2018, 2018.

Kaiser, T. M. Ansorge, J., Arratia, G., Bullwinkel, V., Gunnell, G. F., Herendeen, P. S., Jacobs, B., Mingram, J., Msuya, C., Musolff, A., Naumann, R., Schulz, E. and Wilde, V.: The maar lake of Mahenge (Tanzania) unique evidence of Eocene terrestrial environments in sub-Sahara Africa, Zeitschrift der Deutschen Gesellschaft für Geowissenschaften Band 157 Heft 3, DOI: 10.1127/1860-1804/2006/0157-0411, 2006.

Kaplan, J. O., Bigelow, N. H., Prentice, I. C., Harrison, S. P., Bartlein, P. J., Christensen, T. R., Cramer, W., Matveyeva, N. V., McGuire, A. D., Murray, D. F., Razzhivin, V. Y., Smith, B., Walker, D. A., Anderson, P. M., Andreev, A. A., Brubaker, L. B., Edwards, M. E. and Lozhkin, A. V.: Climate change and Arctic ecosystems: 2. Modeling, paleodata-model comparisons, and future projections, J. Geophys. Res., 108, 8171, doi:10.1029/2002jd002559, 2003.

Keery, J. S., Holden, P. B. and Edwards, N. R.: Sensitivity of the Eocene climate to CO2 and orbital variability, Clim. Past, 14, 215-238, DOI: 10.5194/cp-14-215-2018, 2018

Kennedy-Asser, A. T., Lunt, D. J., Farnsworth, A. and Valdes, P. J.: Assessing mechanisms and uncertainty in modeled climatic change at the Eocene-Oligocene transition, Paleoceanography and Paleoclimatology, 34, 16-34. https://doi.org/10.1029/2018PA003380, 2019.

Laval, K., Sadourny, R. and Serafini, Y.: Land surface processes in a simplified general circulation model, Geophys. Astrophys. Fluid Dyn., 17(1), 129-150, https://doi.org/10.1080/03091928108243677, 1981.

A. N., Quade, J., Dupont-Nivet, G.and Jaeger, J. J.: Asian monsoons in a late Eocene greenhouse world, Nature, 513, 7519, DOI: 10.1038/nature13704, 2014

Li, X., Guo, C., Zhang, Z., Otterå, O. H. and Zhang, R.: PlioMIP2 simulations with NorESM-L and NorESM1-F, Clim. Past, 16, 183-197, https://doi.org/10.5194/cp-16-183-2020, 2020.

Liu, W., Xie, S.-P., Liu, Z. and Zhu, J.: Overlooked possibility of a collapsed Atlantic Meridional Overturning Circulation in warming climate, Science Advances, 3(1), e1601666. https://doi.org/10.1126/sciadv.1601666, 2017.

Liu, X. D., Dong, B. W., Yin, Z. Y., Smith, R. S. and Guo, Q. C.: Continental drift, plateau uplift, and the evolutions of monsoon and arid regions in Asia, Africa, and Australia during the Cenozoic, Science China-Earth Sciences, 62, 1053-1075, DOI: 10.1007/s11430-018-9337-8, 2019.

Lott, F.: Alleviation of stationary biases in a GCM through a mountain drag parameterization scheme and a simple representation of mountain lift forces, Mon. Wea. Rev., 127(5), 788-801, https://doi.org/10.1175/1520-0493(1999)127<0788:AOSBIA>2.0.CO;2, 1999.

Louis, J. F.: A parametric model of vertical eddy fluxes in the atmosphere, Boundary-Layer Meteorol., 17(2), 187-202, https://doi.org/10.1007/BF00117978, 1979.

Lunt, D. J., Bragg, F., Chan, W.-L., Hutchinson, D. K., Ladant, J.-B., Morozova, P., Niezgodzki, I., Steinig, S., Zhang, Z., Zhu, J., Abe-Ouchi, A., Anagnostou, E., de Boer, A. M., Coxall, H. K., Donnadieu, Y., Foster, G., Inglis, G. N., Knorr, G., Langebroek, P. M., Lear, C. H., Lohmann, G., Poulsen, C. J., Sepulchre, P., Tierney, J. E., Valdes, P. J., Volodin, E. M., Dunkley Jones, T., Hollis, C. J., Huber, M. and Otto-Bliesner, B. L.: DeepMIP: model intercomparison of early Eocene climatic optimum (EECO) large-scale climate features and comparison with proxy data, Clim. Past, 17, 203-227, https://doi.org/10.5194/cp-17-203-2021, 2021.

Lunt, D. J., Dunkley Jones, T., Heinemann, M., Huber, M., LeGrande, A., Winguth, A., Loptson, C., Marotzke, J., Roberts, C. D., Tindall, J., Valdes, P. and Winguth, C.: A model-data comparison for a multi-model ensemble of early Eocene atmosphere-ocean simulations: EoMIP, Clim. Past, 8, 1717-1736, https://doi.org/10.5194/cp-8-1717-2012, 2012.

Lunt, D. J., Huber, M., Anagnostou, E., Baatsen, M. L. J., Caballero, R., DeConto, R., Dijkstra, H. A., Donnadieu, Y., Evans, D., Feng, R., Foster, G. L., Gasson, E., von der Heydt, A. S., Hollis, C. J., Inglis, G. N., Jones, S. M., Kiehl, J., Kirtland Turner, S., Korty, R. L., Kozdon, R., Krishnan, S., Ladant, J.-B., Langebroek, P., Lear, C. H., LeGrande, A. N., Littler, K., Markwick, P., Otto-Bliesner, B., Pearson, P., Poulsen, C. J., Salzmann, U., Shields, C., Snell, K., Stärz, M., Super, J., Tabor, C., Tierney, J. E., Tourte, G. J. L., Tripati, A., Upchurch, G. R., Wade, B. S., Wing, S. L., Winguth, A. M. E., Wright, N. M., Zachos, J. C. and Zeebe, R. E.: The DeepMIP contribution to PMIP4: experimental design for model simulations of the EECO, PETM, and pre-PETM (version 1.0), Geosci. Model Dev., 10, 889-901, https://doi.org/10.5194/gmd-10-889-2017, 2017.

Ma, Y. Q., Fan, M. J., Lu, Y. C., Liu, H. M., Zhang, S. P. and Liu, X. F.: Stable isotope record of middle Eocene summer monsoon and its instability in eastern China, Global and Planetary Change, 175, 103-112, DOI: 10.1016/j.gloplacha.2019.02.007, 2019.

Maidment, R. I., Grimes, D., Black, E., Tarnavsky, E., Young, M., Greatrex, H., Allan, R. P., Stein, T., Nkonde, E., Senkunda, S. and Alcántara, E. M. U.: A new, long-term daily satellite-based rainfall dataset for operational monitoring in Africa, nature Scientific Data, 4: 170063. DOI: 10.1038/sdata.2017.63, 2017.

Maidment, R. I., Grimes, D., Allan, R. P., Tarnavsky, E., Stringer, M., Hewison, T., Roebeling, R. and Black, E.: The 30-year TAMSAT African Rainfall Climatology and Time-series (TARCAT) Data Set, J. Geophys. Res.: Atmos., 119(10): 619-610, 644. DOI: 10.1002/2014JD021927, 2014.

Marsland, S. J., Haak, H., Jungclaus, J. H., Latif, M. and Roske, F.: The Max-Planck-Institute global ocean/sea ice model with orthogonal curvilinear coordinates, Ocean Model., 5, 91-127, https://doi.org/10.1016/S1463-5003(02)00015-X, 2003.

Martínez-Botí, M. A., Foster, G. L., Chalk, T. B., Rohling, E. J., Sexton, P. F., Lunt, D. J., Pancost, R. D., Badger, M. P. S. and Schmidt, D. N.: Plio-Pleistocene climate sensitivity evaluated using high-resolution CO_2 records, Nature, 518, 49-54, https://doi.org/10.1038/nature14145, 2015.

Menne, M. J., Durre I., Vose, R. S., Gleason, B. E. and Houston, T. G.: An overview of the Global Historical Climatology Network-Daily Database, J. Atmos. and Oceanic Tech., 29, 897-910, doi.10.1175/JTECH-D-11-00103.1, 2012.

Monerie, P-A., Wainwright, C. M. and Sidibe, M.: Model uncertainties in climate change impacts on Sahel precipitation in ensembles of CMIP5 and CMIP6 simulations, Clim. Dyn., 55, 1385-1401, https://doi.org/10.1007/s00382-020-05332-0, 2020.

Moorthi, S. and Suarez, M. J.: Relaxed Arakawa-Schubert. A Parameterization of Moist Convection for General Circulation Models, Mon. Weather Rev., 120, 978-1002, https://doi.org/10.1175/1520-0493(1992)120<0978:RASAPO>2.0.CO;2, 1992.

Morcrette, J. J., Smith, L. and Fouquart, Y.: Pressure and temperature dependence of the absorption in longwave radiation parameterizations, Beitr. Phys. Atmos., 59, 455-469, ISSN 0005-8173, 1986.

Morrison, H. and Gettelman, A.: A New Two-Moment Bulk Stratiform Cloud Microphysics Scheme in the Community Atmosphere Model, Version 3 (CAM3). Part I: Description and Numerical Tests, J. Clim., 21(15), 3642-3659, DOI:10.1175/2008JCLI2105.1, 2008.

Naafs, B. D. A., Rohrssen, M., Inglis, G. N., Lähteenoja, O., Feakins, S. J., Collinson, M. E., Kennedy, E. M., Singh, P. K., Singh, M. P., Lunt, D. J. and Pancost, R. D.: High temperatures in the terrestrial mid-latitudes during the early Palaeogene, Nature Geosci 11, 766-771, https://doi.org/10.1038/s41561-018-0199-0, 2018.

Neale, R. B., Richter, J. H. and Jochum M.: The impact of convection on ENSO: From a delayed oscillator to a series of events, J. Clim., 21(22), 5904-5924, https://doi.org/10.1175/2008JCLI2244.1, 2008.

Neale, R. B., Richter, J. H., Park, S., Lauritzen, P. H., Vavrus, S. J., Rasch, P. J. and Zhang, M.: The Mean Climate of the Community Atmosphere Model (CAM4) in Forced SST and Fully Coupled Experiments, J. Clim., 26(14), 5150-5168, https://doi.org/10.1175/JCLI-D-12-00236.1, 2013.

Okeke, K. K. and Umeji, O. P.: Palynostratigraphy, palynofacies and palaeoenvironment of deposition of Selandian to Aquitanian sediments, southeastern Nigeria, Journal of African Earth Sciences, 120, 102-124, DOI: 10.1016/j.jafrearsci.2016.04.020, 2016

Park, S. and Bretherton, C. S.: The University of Washington Shallow Convection and Moist Turbulence Schemes and Their Impact on Climate Simulations with the Community Atmosphere Model, J. Clim., 22(12), 3449-3469, DOI:10.1175/2008JCLI2557.1, 2009.

Pearson, P. N., Ditchfield, P. W., Singano, J., Harcourt-Brown, K. G., Nicholas, C. J. and Olsson, R. K.: Warm tropical sea surface temperatures in the Late Cretaceous and Eocene epochs, Nature, 413, 481-487, DOI: 10.1038/35097000, 2001.

Pearson, P. N. and Wade, B. S.: Stable warm tropical climate through the Eocene Epoch, Geology, 35 (1), https://doi.org/10.1130/G24462Y.1, 2007.

Quan, C., Liu, Y. S. and Utescher, T.: Eocene monsoon prevalence over China: A paleobotanical perspective, Palaeogeography Palaeoclimatology Palaeoecology, 365, 302-311, DOI: 10.1016/j.palaeo.2012.09.035, 2012.

Rae, J. W. B., Zhang, Y. G., Liu, X., Foster, G. L., Stoll, H. M. and Whiteford, R. D. M.: Atmospheric CO_2 over the past 66 million years from marine archives, Annual Review of Earth and Planetary Sciences, 49, 606-641, https://doi.org/10.1146/annurev-earth-082420-063026, 2021.

Rasch, P. J. and Kristjánsson, J. E.: A comparison of the CCM3 model climate using diagnosed and predicted condensate parameterizations, J. Clim., 11(7), 1587-1614, https://doi.org/10.1175/1520-0442(1998)011<1587:ACOTCM>2.0.CO;2, 1998.

Reichgelt, T., D'Andrea, W. J. and Fox, B. R. S.: Abrupt plant physiological changes in southern New Zealand at the termination of the Mi-1 event reflect shifts in hydroclimate and pCO_2, EPSL, 455, 115–124, https://doi.org/10.1016/j.epsl.2016.09.026, 2016.

Reichgelt, T., Greenwood, D. R., Steinig, S., Conran, J. G., Scriven, L. J., Zhu, J., Hutchinson, D. K. and Lunt, D. J.: Plant proxy evidence for high rainfall and productivity in the Eocene of Australia, Clim. Past, in Prep.

Richter, J. H. and Rasch, P. J.: Effects of convective momentum transport on the atmospheric circulation in the Community Atmosphere Model, version 3, J. Clim., 21, 1487-1499, https://doi.org/10.1175/2007JCLI1789.1, 2008.

Roeckner, E., Bäuml, G., Bonaventura, L., Brokopf, R., Esch, M., Giorgetta, M., Hagemann, S., Kirchner, I., Kornbleuh, L., Manzini, E., Rhodin, A., Schlese, U., Schulzweida, U. and Tompkins, A.: The atmospheric general circulation model ECHAM 5. PART I: Model description, Report 349, Max-Planck Institut für Meteorologie, Hamburg, Germany, 140 pp., 2003.

Rotstayn, L. D.: A physically based scheme for the treatment of stratiform clouds and precipitation in large-scale models. I: Description and evaluation of the microphysical processes, Q. J. R. Meteorol. Soc., 123, 1227–1282, https://doi.org/https://doi.org/10.1002/qj.49712354106, 1997.

Rougier, J. C., Goldstein, M. and House, L.: Second-order exchangeability analysis for multi-model ensembles, Journal of the American Statistical Association, 108, 852-863, doi:10.1080/01621459.2013.802963, 2013.

Salami, M. B.: Late Cretaceous and Early Tertiary Palynofacies of Southwestern Nigeria, Revista Espanola de Micropaleontologia, XVI, 415-423, 1984.

Salard-Cheboldaeff, M.: Palynologie Maestrichtienne et Tertiaire du Cameroun. Etude qualitative et repartition verticale des principales especes, Review of Palaeobotany and Palynology, 28, 365-388, https://doi.org/10.1016/0034-6667(79)90032-0, 1979.

Salerno, J., Diem, J. E., Konecky, B. L. and Hartter, J.: Recent intensification of the seasonal rainfall 3391 cycle in equatorial Africa revealed by farmer perceptions, satellite-based estimates, and ground-based station 3392 measurements, Climatic Change, 153(1-2):123-139, DOI:10.1007/s10584-019-02370-4, 2019.

Sepulchre, P., Caubel, A., Ladant, J.-B., Bopp, L., Boucher, O., Braconnot, P., Brockmann, P., Cozic, A., Donnadieu, Y., Dufresne, J.-L., Estella-Perez, V., Ethé, C., Fluteau, F., Foujols, M.-A., Gastineau, G., Ghattas, J., Hauglustaine, D., Hourdin, F., Kageyama, M., Khodri, M., Marti, O., Meurdesoif, Y., Mignot, J., Sarr, A.-C., Servonnat, J., Swingedouw, D., Szopa, S. and Tardif, D.: IPSL-CM5A2 – an Earth system model designed for multi-millennial climate simulations, Geosci. Model Dev., 13, 3011-3053, https://doi.org/10.5194/gmd-13-3011-2020, 2020.

Smagorinsky, J.: General Circulation Experiments with the Primitive Equations: I The Basic Experiment, Mon. Weather Rev., 91, 99-164, https://doi.org/10.1175/1520-0493(1963)091<0099:GCEWTP>2.3.CO;2, 1963.

Stepanek, C. and Lohmann, G.: Modelling mid-Pliocene climate with COSMOS, Geosci. Model Dev., 5, 1221-1243, https://doi.org/10.5194/gmd-5-1221-2012, 2012.

Takata, K., Watanabe, T. and Emori, S.: Development of the minimal advanced treatments of surface interaction and runoff, Global Planet. Change, 38, 209-222, doi:10.1016/S0921-8181(03)00030-4, 2003.

Tarnavsky, E., Grimes, D., Maidment, R. I., Black, E., Allan, R. P., Stringer, M., Chadwick, R. and Kayitakire, F.: Extension of the TAMSAT Satellite-based Rainfall Monitoring over Africa and from 1983 to present. J. Applied Meteor. and Climatol., 53(12): 2805-2822. DOI: 10.1175/JAMC-D-14-0016.1, 2014.

Taylor, K. E., Stouffer, R. J. and Meehl, G. A.: An overview of CMIP5 and the experiment design, B. Am. Meteorol. Soc, 93, 485-498, https://doi.org/10.1175/BAMS-D-11-00094.1, 2011.

Tiedtke, M.: Representation of Clouds in Large-Scale Models, Mon. Weather Rev., 121, 3040-3061, https://doi.org/10.1175/1520-0493(1993)121<3040:ROCILS>2.0.CO;2, 1993.

Tierney, J. E., Poulsen, C. J., Montañez, I. P., Bhattacharya, T., Feng, R., Ford, H. L., Hönisch, B., Inglis, G. N., Petersen, S. V., Sagoo, N., Tabor, C. R., Thirumalai, K., Zhu, J., Burls, N. J., Foster, G. L., Goddéris, Y., Huber, B. T., Ivany, L. C., Turner, S. K., Lunt, D. J., McElwain, J. C., Mills, B. J. W., Otto-Bliesner, B. L., Ridgwell, A. and Zhang, Y-G.: Past climates inform our future, Science, 370 (6510), DOI: 10.1126/science.aay3701, 2020.

Tokioka, T., Yamazaki, K., Kitoh, A. and Ose, T.: The Equatorial 30-60 day Oscillation and the Arakawa-Schubert Penetrative Cumulus Parameterization, J. Meteorol. Soc. Japan, 66, 883-901, https://doi.org/10.2151/jmsj1965.66.6_883, 1988.

Utescher, T., Bruch, A. A., Erdei, B., François, L., Ivanov, D., Jacques, F. M. B., Kern, A. K., Liu, Y.-S., Mosbrugger, V. and Spicer, R. A.: The Coexistence Approach - Theoretical background and practical considerations of using plant fossils for climate quantification, Palaeogeography, Palaeoclimatology, Palaeoecology, 410, 58-73, https://doi.org/10.1016/j.palaeo.2014.05.031, 2014.

Uzodimma, D. E.: Palynostratigraphy, Age Determination and Depositional Environments of the Imo Shale Exposures at the Okigwe/Port Harcourt Express Road Junction Okigwe, Southeastern Nigeria, Greener Journal of Physical Sciences, 3, 255-272, ISSN: 2276-7851, 2013.

van Dijk, J., Fernandez, A., Bernasconi, S. M., Caves Rugenstein, J. K., Passey, S. R. and White, T.: Spatial pattern of super-greenhouse warmth controlled by elevated specific humidity, Nat. Geosci., 13, 739–744, https://doi.org/10.1038/s41561-020-00648-2, 2020.

Valdes, P. J., Armstrong, E., Badger, M. P. S., Bradshaw, C. D., Bragg, F., Crucifix, M., Davies-Barnard, T., Day, J. J., Farnsworth, A., Gordon, C., Hopcroft, P. O., Kennedy, A. T., Lord, N. S.,

Lunt, D. J., Marzocchi, A., Parry, L. M., Pope, V., Roberts, W. H. G., Stone, E. J., Tourte, G. J. L. and Williams, J. H. T.: The BRIDGE HadCM3 family of climate models: HadCM3@Bristol v1.0, Geosci. Model Dev., 10, 3715-3743, https://doi.org/10.5194/gmd-10-3715-2017, 2017.

Volodin, E. M. and Lykossov, V. N.: Parameterization of Heat and Moisture Transfer in the Soil-Vegetation System for Use in Atmospheric General Circulation Models: 2. Numerical Experiments in Climate Modeling, Izvestiya Atmospheric and Oceanic Physics, 34(5), 559-569, 1998.

Volodin, E. M., Mortikov, E. V., Kostrykin, S. V., Galin, V. Y., Lykossov, V. N., Gritsun, A. S., Diansky, N. A., Gusev, A. V. and Iakovlev, N. G.: Simulation of the present-day climate with the climate model INMCM5, Clim. Dynam., 49, 3715-3734, 10.1007/s00382-017-3539-7, 2017.

Volodin, E. M., Mortikov, E. V., Kostrykin, S. V., Galin, V. Y., Lykossov, V. N., Gritsun, A. S., Diansky, N. A., Gusev, A. V., Iakovlev, N. G., Shestakova, A. A. and Emelina, S. V.: Simulation of the modern climate using the INMCM48 climate model, Russ. J. Numer. Anal. M., 33, 367-374, https://doi.org/10.1515/rnam-2018-0032, 2018.

West, C. K., Greenwood, D. R., Reichgelt, T., Lowe, A. J., Vachon, J. M., and Basinger, J. F.: Paleobotanical proxies for early Eocene climates and ecosystems in northern North America from middle to high latitudes, Clim. Past, 16, 1387-1410, https://doi.org/10.5194/cp-16-1387-2020, 2020.

Westerhold, T., Marwan, N., Drury, A. J., Liebrand, D., Agnini, C., Anagnostou, E., Barnet, J. S. K., Bohaty, S. M., De Vleeschouwer, D., Florindo, F., Frederichs, T., Hodell, D. A., Holbourn, A. E., Kroon, D., Lauretano, V., Littler, K., Lourens, L. J., Lyle, M., Pälike, H., Röhl, U., Tian, J., Wilkens, R. H., Wilson, P. A. and Zachos, J. C.: An astronomically dated record of Earth's climate and its predictability over the last 66 million years, Science, 369(6509), 1383-1387, https://doi.org/10.1126/science.aba6853, 2020.

Wilf, P., Wing, S. L., Greenwood, D. R. and Greenwood, C. L.: Using fossil leaves as paleoprecipitation indicators: An Eocene example, Geology, 26, 203-206, https://doi.org/10.1130/0091-7613(1998)026<0203:UFLAPI>2.3.CO;2, 1998.

Williams, C. J. R., Guarino, M.-V., Capron, E., Malmierca-Vallet, I., Singarayer, J. S., Sime, L. C., Lunt, D. J. and Valdes, P. J.: CMIP6/PMIP4 simulations of the mid-Holocene and Last Interglacial using HadGEM3: comparison to the pre-industrial era, previous model versions and proxy data, Clim. Past, 16, 1429-1450, https://doi.org/10.5194/cp-16-1429-2020, 2020.

Williams, C. J. R. and Kniveton, D. R. (eds). African Climate and Climate Change: Physical, Social and Political Perspectives. Springer Science+Business Media BV 2011. Dordrecht, Heidelberg, London and New York: 212pp. DOI: 10.1007/978-90-481-3842-5, 2011.

Williams, C. J. R., Kniveton, D. R. and Layberry, R.: Climatic and oceanic associations with daily rainfall extremes over southern Africa, Int. J. Clim., 27 (1): 93-108, https://doi.org/10.1002/joc.1376, 2007.

Williams, C. J. R., Kniveton, D. R. and Layberry, R.: Influence of South Atlantic sea surface temperatures on rainfall variability and extremes over southern Africa, J. Clim., 21: 6498-6520, DOI: https://doi.org/10.1175/2008JCLI2234.1, 2008.

Williams, C. J. R., Kniveton, D. R. and Layberry, R.: Assessment of a climate model to reproduce rainfall variability and extremes over southern Africa, Theor. Applied Climatol., 99: 9-27, DOI: 10.1007/s00704-009-0124-y, 2010.

Williams, C. J. R., Sellar, A. A., Ren, X., Haywood, A. M., Hopcroft, P., Hunter, S. J., Roberts, W. H. G., Smith, R. S., Stone, E. J., Tindall, J. C., and Lunt, D. J.: Simulation of the mid-Pliocene Warm Period using HadGEM3: experimental design and results from model–model and model–data comparison, Clim. Past, 17, 2139-2163, https://doi.org/10.5194/cp-17-2139-2021, 2021.

Willard, D. A., Donders, T. H., Reichgelt, T., Greenwood, D. R., Sangiorgi, F., Peterse, F., Nierop, K. G. J., Frieling, J., Schouten, S. and Sluijs, A.: Arctic vegetation, temperature, and hydrology during Early Eocene transient global warming events, Global and Planetary Change, 178, 139-152, https://doi.org/10.1016/j.gloplacha.2019.04.012, 2019.

Wright, I. J., Dong, N., Maire, V., Prentice, I. C., Westoby, M., Díaz, S., Gallagher, R. V., Jacobs, B. F., Kooyman, R., Law, E. A., Leishman, M. R., Niinemets, U., Reich, P. B., Sack, L., Villar, R., Wang, H. and Wilf, P.: Global climatic drivers of leaf size, Science, 357(6354), 917–921, DOI: 10.1126/science.aal4760, 2017.

Xie, Y. L., Wu, F. L. and Fang, X. M.: Middle Eocene East Asian monsoon prevalence over southern China: Evidence from palynological records, Global and Planetary Change, 175, 13-26, DOI: 10.1016/j.gloplacha.2019.01.019, 2019.

Zhang, G. J. and McFarlane, N. A.: Sensitivity of climate simulations to the parameterization of cumulus convection in the Canadian Climate Centre general circulation model, Atmosphere–Ocean, 33(3), 407-446, https://doi.org/10.1080/07055900.1995.9649539, 1995.

Zhang, M., Lin, W., Bretherton, C. S., Hack, J. J. and Rasch, P. J.: A modified formulation of fractional stratiform condensation rate in the NCAR Community Atmospheric Model (CAM2), J. Geophys. Res., 108(D1), 4035, https://doi.org/10.1029/2002JD002523, 2003.

Zhu, J., Poulsen, C. J. and Otto-Bliesner, B. L.: High climate sensitivity in CMIP6 model not supported by paleoclimate, Nat. Clim. Chang, 10, 378-379, https://doi.org/10.1038/s41558-020-0764-6, 2020.